

Lattice Boltzmann Model for Transonic Flows

M. Atif,¹ N. H. Maruthi,² P. K. Kolluru,² C. Thantanapally,² and S. Ansumali³

¹*Brookhaven National Laboratory, Upton, New York 11973, USA*

²*Sankhyasutra Labs, Bangalore 560064, India*

³*Jawaharlal Nehru Centre for Advanced Scientific
Research, Jakkur, Bangalore 560064, India*

Abstract

The hydrodynamic limit of a discrete kinetic equation is intrinsically connected with the symmetry of the lattices used in construction of a discrete velocity model. On mixed lattices composed of standard lattices the sixth-order (and higher) moment is often not isotropic and thus they are insufficient to ensure correct imposition of the hydrodynamic moments. This makes the task of developing lattice Boltzmann model for transonic flows quite challenging. We address this by decoupling the physical space lattice from the velocity space lattice to construct a lattice Boltzmann model with very high isotropy. The model is entirely on-lattice like the isothermal models, achieves a Mach number of two with only 81 discrete velocities, and admits a simple generalization of equilibrium distribution used in isothermal equilibrium. We also present a number of realistic benchmark problems to show that the lattice Boltzmann model with a limited number of velocities is not only feasible for transonic flow but is also quite simple and efficient like its subsonic counterpart.

I. INTRODUCTION

The lattice Boltzmann model (LBM), a discrete kinetic scheme, is an efficient method to compute solutions to the Boltzmann equation (BE) in a regime of small deviations from the equilibrium state around rest and isothermal condition described by a fixed reference temperature. Even though its standard formulations describe compressible (subsonic and isothermal) fluids on standard lattices (19 or 27 discrete velocities in three-spatial dimensions), the LBM has arguably achieved most of its success and utility in areas with complex and coupled physics in the realm of extreme subsonic and isothermal flows where incompressibility is a good approximation [1–8]. Although the higher-order (multispeed) models have extended the method even for moderate (but still subsonic) Mach number hydrodynamics, LBMs for compressible flows are yet to mature [9–16]. Despite recent progress [9, 11, 17, 18], the same can also be said for LBM with energy conservation when the imposed thermal gradients are strong. The essential reason for the failure of lower order LBM for strong temperature gradients or high Mach numbers is the perturbative nature of the method and lack of higher order isotropy, which are also its strength at low Mach numbers. The simplicity of this procedure and economy in the choice of a number of discrete velocities makes it a method of choice for solving the Boltzmann BGK equation at a low Mach number.

The challenge is to extend this process for high Mach number flow at a manageable number of discrete velocities with purely Lagrangian on-lattice streaming. However, for compressible flow where the Mach number can be order one, the required number of discrete velocities is often prohibitively large (sometimes as high as 343), which is a major impediment to the development of LBM as a viable scheme for transonic flows.

The choice of lattice Boltzmann method for any application crucially depends on two factors: isotropy of the lattice and equilibrium distribution. Both these essentially originate from the fact that in the basic formulation of LBM, the local equilibrium distribution $f^{\text{eq}}(\mathbf{v}, \mathbf{u}, \theta)$ for molecular velocity \mathbf{v} at fluid velocity \mathbf{u} and temperature θ is written in series form in powers of Mach number ($\text{Ma} = |\mathbf{u}|/c_s$) where c_s is the sound speed. This series is expanded around the rest state Maxwell-Boltzmann distribution $f^{\text{MB}}(\mathbf{u} = \mathbf{0}, \theta_0) \equiv W(\theta_0)$ at a fixed temperature θ_0 (typically till second order) as

$$f^{\text{eq}}(\mathbf{v}, \mathbf{u}) = W(\theta_0) \left[1 + \frac{\mathbf{u} \cdot \mathbf{v}}{\theta_0} + \frac{(\mathbf{v} \cdot \mathbf{u})^2 - u^2 \theta_0}{2\theta_0^2} \right]. \quad (1)$$

The second order is sufficient to recover the subsonic isothermal limit of hydrodynamics as only the correct form of pressure tensor is needed in this limit [19]. This continuous form of the expanded equilibrium is then evaluated on the quadrature nodes \mathbf{c}_i to obtain $O(\text{Ma}^3)$ accurate form of discrete equilibrium as

$$f^{\text{eq}}(\mathbf{c}_i, \mathbf{u}) = W_i(\theta_0) \left[1 + \frac{\mathbf{u} \cdot \mathbf{c}_i}{\theta_0} + \frac{(\mathbf{c}_i \cdot \mathbf{u})^2 - u^2 \theta_0}{2\theta_0^2} \right], \quad (2)$$

where i represents a discrete velocity. The weights $W_i(\theta_0) \equiv w_i$ ($w_i \geq 0$) for the discrete velocity analogue and second-order accuracy of the pressure tensor get translated as the condition on the isotropy of the velocity set and associated weights as [20, 21]

$$\sum_i w_i = 1, \quad \sum_i w_i c_{i\alpha} c_{i\beta} = \theta_0 \delta_{\alpha\beta}, \quad \sum_i w_i c_{i\alpha} c_{i\beta} c_{i\gamma} c_{i\kappa} = \theta_0^2 \Delta_{\alpha\beta\gamma\kappa}, \quad (3)$$

where $\delta_{\alpha\beta}$ is the Kronecker delta and $\Delta_{\alpha\beta\gamma\kappa} = \delta_{\alpha\beta}\delta_{\gamma\kappa} + \delta_{\alpha\gamma}\delta_{\beta\kappa} + \delta_{\alpha\kappa}\delta_{\beta\gamma}$ is the isotropic generalized Kronecker delta function. Imposing these isotropy conditions in itself is a non-trivial task on standard lattices as the fourth-order moment of individual lattices is not

isotropic on a lattice of single type [20–23]. In particular

$$\begin{aligned}
\sum_{i \in \mathcal{S}} \frac{c_{i\alpha} c_{i\beta} c_{i\gamma} c_{i\kappa}}{c^4} &= 2 \delta_{\alpha\beta\gamma\kappa}, \\
\sum_{i \in \mathcal{F}} \frac{c_{i\alpha} c_{i\beta} c_{i\gamma} c_{i\kappa}}{c^4} &= -4 \delta_{\alpha\beta\gamma\kappa} + 4 \Delta_{\alpha\beta\gamma\kappa}, \\
\sum_{i \in \mathcal{B}} \frac{c_{i\alpha} c_{i\beta} c_{i\gamma} c_{i\kappa}}{c^4} &= -16 \delta_{\alpha\beta\gamma\kappa} + 8 \Delta_{\alpha\beta\gamma\kappa},
\end{aligned} \tag{4}$$

where, $\delta_{\alpha\beta\gamma\kappa}$ is the anisotropic component leading to a loss of isotropy and $\mathcal{S}, \mathcal{F}, \mathcal{B}$ are sets of discrete velocities in simple cubic (SC), face-centered cubic (FCC), and body-centered cubic (BCC) shells respectively. Here, we remind that the standard choices of velocity space lattice in three dimensions comprise SC, FCC, and BCC shells [see Appendix A for more information on shells and their isotropy conditions derivation]. The lattice Boltzmann method in its present form evolved from the observation that in Eq.(4) anisotropic components have an opposite sign, and thus, it is possible to give different weights to various shells to make the resulting combination fully isotropic at the fourth order with D3Q15, D3Q19 and D3Q27 models being the most prominent ones. Indeed, many multispeed lattices also exist where higher isotropy can be obtained with positive weights [23–27].

It is evident from the series form in equilibrium in Eq. (1) that one requires higher order contributions for high Mach number case (even at constant temperature). However, that often requires matching higher moments of Maxwell–Boltzmann distribution and would thus require more velocity shells [9, 11, 28]. Any attempt to model transonic flows has to ensure that not only the fourth order moment but also the sixth order as well as once contracted 8th-order moment of the discrete velocity model are isotropic [29]. This is a non-trivial condition as all three fundamental components of the discrete velocity model (SC, FCC, BCC) shells are highly anisotropic at the sixth order. This is evident from the explicit expression

$$\begin{aligned}
\sum_{i \in \mathcal{S}} \frac{c_{i\alpha} c_{i\beta} c_{i\gamma} c_{i\kappa} c_{i\eta} c_{i\zeta}}{2 c^6} &= \delta_{\alpha\beta\gamma\kappa\eta\zeta} \\
\sum_{i \in \mathcal{F}} \frac{c_{i\alpha} c_{i\beta} c_{i\gamma} c_{i\kappa} c_{i\eta} c_{i\zeta}}{4 c^6} &= -13 \delta_{\alpha\beta\gamma\kappa\eta\zeta} + \delta_{\alpha\beta\gamma\kappa\eta\zeta}^{(4,2)} \\
\sum_{i \in \mathcal{B}} \frac{c_{i\alpha} c_{i\beta} c_{i\gamma} c_{i\kappa} c_{i\eta} c_{i\zeta}}{8 c^6} &= 16 \delta_{\alpha\beta\gamma\kappa\eta\zeta} - 2 \delta_{\alpha\beta\gamma\kappa\eta\zeta}^{(4,2)} + \Delta_{\alpha\beta\gamma\kappa\eta\zeta},
\end{aligned} \tag{5}$$

where $\Delta_{\alpha\beta\gamma\kappa\eta\zeta}$ is the isotropic tensor and $\delta_{\alpha\beta\gamma\kappa\eta\zeta}^{(4,2)}$ is the anisotropic product of Kronecker delta and fourth-order anisotropic tensor. Similarly, for once contracted 8th moment, we

have

$$\begin{aligned}
\sum_{i \in \mathcal{S}} \frac{c_i^2 c_{i\alpha} c_{i\beta} c_{i\gamma} c_{i\kappa} c_{i\eta} c_{i\zeta}}{2 c^8} &= \delta_{\alpha\beta\gamma\kappa\eta\zeta} \\
\sum_{i \in \mathcal{F}} \frac{c_i^2 c_{i\alpha} c_{i\beta} c_{i\gamma} c_{i\kappa} c_{i\eta} c_{i\zeta}}{8 c^8} &= -13 \delta_{\alpha\beta\gamma\kappa\eta\zeta} + \delta_{\alpha\beta\gamma\kappa\eta\zeta}^{(4,2)} \\
\sum_{i \in \mathcal{B}} \frac{c_i^2 c_{i\alpha} c_{i\beta} c_{i\gamma} c_{i\kappa} c_{i\eta} c_{i\zeta}}{24 c^8} &= 16 \delta_{\alpha\beta\gamma\kappa\eta\zeta} - 2 \delta_{\alpha\beta\gamma\kappa\eta\zeta}^{(4,2)} + \Delta_{\alpha\beta\gamma\kappa\eta\zeta}.
\end{aligned} \tag{6}$$

Thus, we obtain obvious relations to ensure isotropy at various orders listed in Table I. Essential technical difficulty originates from the fact that numerical simplicity demands LBM to work with fixed grid in velocity space which implies that components of \mathbf{c}_i are integers. It is evident from Table I that satisfying these complicated constraints is not possible on lower-order lattices and is a challenge on higher-order lattices. Previous works have demonstrated that introducing a replica grid which allows \mathbf{c}_i to take values of half (see Fig. 1) allows one to construct discrete velocity models that follow isotropy up to a much higher level while retaining the conceptual simplicity of LBM [11, 12, 30].

4 th order isotropy	$2 \sum_{i \in \mathcal{S}} w_i c_i^4 - 4 \sum_{i \in \mathcal{F}} w_i c_i^4 - 16 \sum_{i \in \mathcal{B}} w_i c_i^4 = 0$
6 th order isotropy	$2 \sum_{i \in \mathcal{S}} w_i c_i^6 - 52 \sum_{i \in \mathcal{F}} w_i c_i^6 + 128 \sum_{i \in \mathcal{B}} w_i c_i^6 = 0$ $4 \sum_{i \in \mathcal{F}} w_i c_i^6 - 16 \sum_{i \in \mathcal{B}} w_i c_i^6 = 0$
Once-contracted 8 th order isotropy	$2 \sum_{i \in \mathcal{S}} w_i c_i^8 - 104 \sum_{i \in \mathcal{F}} w_i c_i^8 - 384 \sum_{i \in \mathcal{B}} w_i c_i^8 = 0$ $8 \sum_{i \in \mathcal{F}} w_i c_i^8 - 48 \sum_{i \in \mathcal{B}} w_i c_i^8 = 0$
Thrice-contracted 10 th order isotropy	$2 \sum_{i \in \mathcal{S}} w_i c_i^{10} - 32 \sum_{i \in \mathcal{F}} w_i c_i^{10} - 432 \sum_{i \in \mathcal{B}} w_i c_i^{10} = 0$

TABLE I: Conditions on the discrete velocities and shells to satisfy isotropy at the various orders.

In this paper, we derive one such higher-order model that satisfies all the constraints listed in Table I. The key set of ideas used in this work to construct such a higher-order model for transonic flow are:

- **Physical space lattice vs velocity space lattice:** It was first argued in Ref. [31] that the lattice in physical space need not be tied up to the lattices created by the link of discrete velocities. It was pointed out that the constraint on the moment exists only in the velocity space lattice, and the choice of simple cubic lattice in physical space is

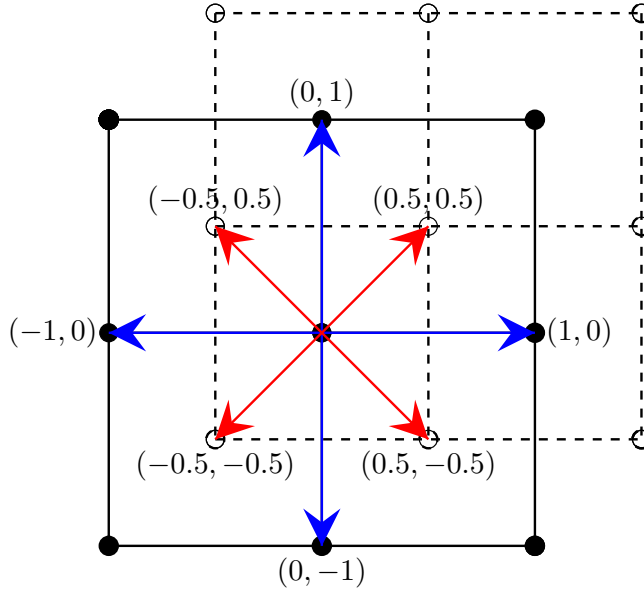


FIG. 1: Illustration of a staggered replica grid and half-links that improve the flexibility for imposing required isotropy conditions.

only needed to preserve the Lagrangian nature of the numerical scheme, which makes it highly efficient and non-dissipative. Namburi *et al.* [30] illustrated that the replica lattice in physical space brings more flexibility and accuracy by allowing c_i to take values of half on a staggered replica grid (see Fig. 1 for illustration).

- **Entropic equilibrium and temperature-dependent weights:** Energy conserving LBMs require that pressure, stress, and heat fluxes are thermodynamically consistent and remain accurate up to a high order [11, 32]. This requires that the local pressure is the product of local temperature and density and that deviatoric stress and heat fluxes at equilibrium have minimal errors. For large deviations, we also present an algorithm for efficient evaluation of the true entropic equilibrium which is constructed as the minimizer of the Boltzmann's entropy. We do so by assembling a 5×5 linear system and solving for the Lagrange multipliers. We present a series form of equilibrium which is an intuitive generalization of isothermal equilibrium. A crucial innovation in our approach is the introduction of temperature-dependent weights $W_i(\theta)$. Existing works use a single expansion in two variables (velocity and temperature) [29, 33, 34] whereas our approach first calculates $W_i(\theta)$ as an series expansion in temperature deviation followed by an expansion in velocity. We know from Ref. [11] that this is better

for flows with strong thermal deviations as it provides accurate initial values of the Lagrange multiplier for solving the linear system.

- **Benchmark problems:** We select a broad range of benchmark problems to evaluate the accuracy of the proposed model. We start by testing the theoretical accuracy on well-known setups such as Sod shock tube and Riemann problems and simulate the transonic cavity which is a problem of high practical relevance in the aerodynamic engineering industry.

The rest of the paper is organized as follows – in Sec. II we briefly review the basics of LBM method and the existing higher-order lattices. In Sec. III we list the constraints, derive the model for transonic flows, and calculate the entropic equilibrium. This is followed by a rigorous benchmark of the model by simulating challenging transonic flows in Sec. IV. Finally, in Sec. V we provide an outlook by discussing the future of higher-order lattices.

II. LATTICE BOLTZMANN METHOD

The set of basic variables in the lattice Boltzmann equation consists of N_d discrete populations $f_i(\mathbf{x}, t)$ of discrete velocities \mathbf{c}_i ($i = 0, 1, 2, \dots, N_d - 1$) at location \mathbf{x} and time t . The hydrodynamic variables, the mass density ρ , the fluid velocity \mathbf{u} , and temperature θ , are related to the the distribution function as

$$\rho = \langle f, \tilde{\mathbf{1}} \rangle \quad \rho u_\alpha = \langle f, c_\alpha \rangle, \quad \rho u^2 + 3\rho\theta = \langle f, c^2 \rangle, \quad (7)$$

where $\tilde{\mathbf{1}}$ is the unit vector of length N_d and the bilinear action $\langle \phi, \psi \rangle = \sum_{i=0}^{N_d-1} \phi_i \psi_i$. Here, we use a scaled temperature θ defined in terms of Boltzmann constant k_B and mass of the particle m as $\theta = k_B T / m$ and the discrete velocities \mathbf{c}_i are in the unit of $\sqrt{k_1 \theta_0}$ where k_1 is a lattice-dependent constant and θ_0 is the base temperature of the lattice. For these models, it is important that zero velocity equilibrium at fixed temperature are positive (i.e. the weights $w_i > 0$) and satisfies the condition that their lower order moments are the same as the moments of Maxwell-Boltzmann distribution. As discussed in Sec. I, this can be imposed by demanding isotropy of the lattice and ensuring the traces at the various orders are same as that of Maxwell-Boltzmann distribution. For example, let us consider the fourth-order isotropy of the the three shells, i.e, $\mathcal{S} = \{(\pm m, 0, 0), (0, \pm m, 0), (0, 0, \pm m)\}$,

$\mathcal{F} = \{(\pm n, \pm n, 0), (\pm n, 0, \pm n), (0, \pm n, \pm n)\}$, $\mathcal{B} = \{(\pm p, \pm p, \pm p)\}$ and weights w_s , w_f and w_b respectively. Then we have the fourth-order isotropy condition as

$$2 w_s m^4 - 4 w_f n^4 - 16 w_b p^4 = 0, \quad (8)$$

and the fourth-order trace from Eq.(3) as

$$\langle w, c^4 \rangle = 6 w_s m^4 + 48 w_f n^4 + 72 w_b p^4 = 15\theta_0^2. \quad (9)$$

In the literature, we frequently find the use of models like *D3Q15* and *D3Q19* that have with $m = n = p = 1$ and impose only the fourth-order isotropy and trace (see Table IV for the weights and velocities and Table VI for the errors in the non-imposed moments). It is straightforward to extend the above idea to multispeed lattices that have m, n, p as sets of natural numbers. It is worth pointing out here that in replica lattices m, n, p can be 0.5, 1.5, 2.5 and so on [11, 12, 30]. Similarly, at the sixth order one obtains the isotropy conditions

$$\begin{aligned} 2 w_s m^6 - 52 w_f n^6 + 128 w_b p^6 &= 0, \\ 4 w_s m^6 - 16 w_b n^6 &= 0, \end{aligned} \quad (10)$$

and the sixth-order trace as

$$\langle w, c^6 \rangle = 6 w_s m^6 + 96 w_f n^6 + 216 w_b p^6 = 105\theta_0^3. \quad (11)$$

It is evident that constructing a discrete velocity set that satisfies Eqs. (8) – (11) is a non-trivial task.

The *D3Q27* model has the full fourth-order as well as one component of the sixth-order moment $\langle w, c_x^2 c_y^2 c_z^2 \rangle$ imposed. The non-imposed moments at the sixth-order contribute to errors for *D3Q15* and *D3Q19* model some of which are absent for the *D3Q27* model. The Zero-One-Three (ZOT) lattice developed by Chikatamarla and Karlin has been frequently used for turbulent flows [25]. The full ZOT lattice has 125 discrete links (*D3Q125*), whereas the pruned one has 41 discrete links (*D3Q41*). The *D3Q41* lattice imposes the fully-expanded sixth-order tensor, and thus has zero error at the contracted sixth orders, whereas the *D3Q125* lattice imposes some moments at the eighth and tenth orders too. In the aforementioned lattices the moments imposed at the higher order are mostly from the fully expanded set of moments. Such lattices work well for turbulent flows but have not

yet found widespread acceptance for simulating flows with large temperature variation or at high Mach number. It should be noted that all odd moments are zero and that imposing the fully contracted tensor $\langle w, c^{2n} \rangle$ for any integer n is equivalent to imposing $\langle w, c^{2(n-1)} c_x^2 \rangle$ due to the underlying isotropy and $c^2 = c_x^2 + c_y^2 + c_z^2$.

To minimize the number of discrete velocities, in the replica lattices the imposed moments are chosen from the contracted set. The development of lattices like *RD3Q41* and *RD3Q67* emphasized the importance of imposing trace of the higher-order moments. Here, *R* represents “replica” as these lattices make use of staggered grid and contain links with magnitude 0.5 [11, 12, 30]. The key idea behind the development of replica lattices was their optimal discretization of position space, with an additional advantage that they offer more freedom to impose moments as these lattices are not derived from the Gauss-Hermite quadrature. In Ref. [11], it was shown that while the sixth-order isotropy of the reference equilibrium (at zero velocity and reference temperature) is a must, one only requires the trace of the eighth and tenth-order moments to match with their corresponding Maxwell-Boltzmann values for accurately simulating thermal flows. Thus, along with the lower order moments, if we demand the isotropy at the sixth order and traces of the sixth and eighth-order moments match the Maxwell-Boltzmann moments we obtain the *RD3Q41* lattice which has been found suitable for mildly thermal and weakly-compressible flows. In addition to the above moments, if we impose isotropy at twice contracted eights order $\sum_i c_i^4 c_{i\alpha} c_{i\beta} c_{i\gamma} c_{i\kappa}$ and traces at the eight order and tenth-order moment we obtain the *RD3Q67* lattice which remains accurate for temperature deviations as large as 50% from the base temperature θ_0 .

Once the velocity space is discretized into a discrete velocity set satisfying the moments of weights as discussed above, one works with the populations f corresponding to each direction as the basic working element. The physical space is discretized into a series of grid nodes that are linked together by the discrete velocity directions. At any point on the lattice, the neighboring nodes are located at distance of $\Delta x = m \mathbf{c}_i \Delta t$, where m is a natural number [4]. This feature of LBM allows for construction of a computationally attractive algorithm where f_i successively streams along the grid and collides at the nodes. Thereafter, the evolution equation reads

$$f_i(\mathbf{x} + \mathbf{c}_i \Delta t, t + \Delta t) = f_i(\mathbf{x}, t) + \alpha \beta [f_i^{\text{eq}}(\rho, \mathbf{u}) - f_i(\mathbf{x}, t)], \quad (12)$$

where $\alpha = 2$ and $\beta = \Delta t / (2\tau + \Delta t)$ is related to the kinematic viscosity ν via relaxation time

$\tau = \nu/\theta_0$, with θ_0 as the reference temperature. The above equation can also be derived by trapezoidal integration of discrete velocity model with BGK collision [35]. The entropic formulation of LBM has an extra step where α is found as the root of the entropy estimate

$$H[f(\mathbf{x}, t) + \alpha (f^{\text{eq}}(\rho, \mathbf{u}, \theta) - f(\mathbf{x}, t))] - H[f(\mathbf{x}, t)] = 0, \quad (13)$$

where H is a convex entropy function. It restores the thermodynamic consistency embedded in the Boltzmann description [32, 36–38]. This method ensures H theorem for discrete space-time formulation, and thus leads to a nonlinearly stable solver that is effective in context of flows with sharp gradients. Thus, entropic LBM is quite suitable for the case of thermal and compressible flows where gradients can be sharp [39]. Various numerical techniques have been proposed to ensure the correctness and efficient implementation of this step [40–47]. The closed form analytical expression for α was found in Ref. [36].

III. TRANSONIC MODEL AND DISCRETE ENTROPIC EQUILIBRIUM

The choice of the discrete equilibrium distribution $f_i^{\text{eq}}(\rho, \mathbf{u}, \theta)$ is considered crucial in LBM. It is known that in order to get the correct thermohydrodynamic limit, the moments of equilibrium distribution should match the moments of the Maxwell-Boltzmann distribution [11]. The conditions on the moments of the equilibrium translate to constraints on the weights, discrete velocities, and the reference temperature θ_0 . In general, the higher the order of the moments imposed, the more accurate is the model. In the previous section, we listed the constraints on some well-known lattices and two recently developed replica lattices for compressible and thermal flows. The conditions on isotropy and traces discussed in the previous section are extended to a higher order to design lattices that remain accurate at higher temperature deviations and transonic flows. The large deviation of stresses in transonic flows require isotropy of the lattice at fourth, sixth, once-contracted eighth order $\sum_i c_i^2 c_{i\alpha} c_{i\beta} c_{i\gamma} c_{i\kappa} c_{i\eta} c_{i\zeta}$, and thrice-contracted tenth-order $\sum_i c_i^6 c_{i\alpha} c_{i\beta} c_{i\gamma} c_{i\kappa}$ explicitly written

as

$$\begin{aligned}
2 \sum_{i \in \mathcal{S}} w_i c_i^4 - 4 \sum_{i \in \mathcal{F}} w_i c_i^4 - 16 \sum_{i \in \mathcal{B}} w_i c_i^4 &= 0, \\
2 \sum_{i \in \mathcal{S}} w_i c_i^6 - 52 \sum_{i \in \mathcal{F}} w_i c_i^6 + 128 \sum_{i \in \mathcal{B}} w_i c_i^6 &= 0, \\
4 \sum_{i \in \mathcal{F}} w_i c_i^6 - 16 \sum_{i \in \mathcal{B}} w_i c_i^6 &= 0, \\
2 \sum_{i \in \mathcal{S}} w_i c_i^8 - 104 \sum_{i \in \mathcal{F}} w_i c_i^8 - 384 \sum_{i \in \mathcal{B}} w_i c_i^8 &= 0, \\
8 \sum_{i \in \mathcal{F}} w_i c_i^8 - 48 \sum_{i \in \mathcal{B}} w_i c_i^8 &= 0, \\
2 \sum_{i \in \mathcal{S}} w_i c_i^{10} - 32 \sum_{i \in \mathcal{F}} w_i c_i^{10} - 432 \sum_{i \in \mathcal{B}} w_i c_i^{10} &= 0,
\end{aligned} \tag{14}$$

along with the traces up to the tenth-order moment

$$\begin{aligned}
\langle w, 1 \rangle &= 1, \langle w, c^2 \rangle = 3\theta_0, \langle w, c^4 \rangle = 15\theta_0^2 \\
\langle w, c^6 \rangle &= 105\theta_0^3, \langle w, c^8 \rangle = 945\theta_0^4, \langle w, c^{10} \rangle = 10395\theta_0^5.
\end{aligned} \tag{15}$$

These conditions can be satisfied on an 81 link model which is developed in this paper and referred to as *RD3Q81*. This model is accurate for transonic as well as strongly thermal flows. As the total number of constraints is twelve, we require ten energy shells whose weights along with w_0 and θ_0 make a total of twelve unknowns. The energy shells chosen are 4 SC, 2 FCC and 4 BCC. The set of equations has many solutions and we accept the one that satisfies the condition that $w_i > 0$ and real. The discrete velocities and weights corresponding to each shell is listed in the Table V.

Next, we derive the energy conserving discrete entropic equilibrium as the minimizer of the entropy function. We begin with the convex entropy function of the Boltzmann form

$$H = \left\langle f_i, \log \left(\frac{f_i}{w_i} \right) - 1 \right\rangle, \tag{16}$$

and construct equilibrium as its minimizer under the constraints of local conservation laws [Eq. (7)]. The formal solution to the minimization problem is

$$f_i^{\text{eq}} = w_i \rho \exp \left(\mu + \zeta_x c_{ix} + \zeta_y c_{iy} + \zeta_z c_{iz} + \gamma c_i^2 \right), \tag{17}$$

where $\mu, \zeta_\kappa, \gamma$ are the Lagrange multipliers associated with mass, momentum and energy respectively. To obtain the discrete equilibrium in terms of the hydrodynamic fields we

need to evaluate the Lagrange multipliers in terms of ρ, u_κ, θ . These Lagrange multipliers can be evaluated explicitly in terms of conserved moments for the models *D1Q3*, *D2Q9*, *D3Q27*. For all other models, in practice, they are calculated numerically by first writing the Lagrange multipliers as perturbation series and taking only the leading-order terms, i.e.,

$$f_i^{\text{eq}} = \tilde{f}_i^{\text{eq}} \exp(\hat{\mu} + \hat{\zeta}_x c_{ix} + \hat{\zeta}_y c_{iy} + \hat{\zeta}_z c_{iz} + \hat{\gamma} c_i^2), \quad (18)$$

where $\hat{\mu}, \hat{\zeta}_x, \hat{\zeta}_y, \hat{\zeta}_z, \hat{\gamma}$ are the deviations for the Lagrange multipliers and

$$\tilde{f}_i^{\text{eq}} = w_i \rho \exp(\mu^{(0)} + \zeta_x^{(0)} c_{ix} + \zeta_y^{(0)} c_{iy} + \zeta_z^{(0)} c_{iz} + \gamma^{(0)} c_i^2) \quad (19)$$

with the guesses $\mu^{(0)}, \zeta_x^{(0)}, \zeta_y^{(0)}, \zeta_z^{(0)}, \gamma^{(0)}$. Thereafter, exploiting the approximation $\exp(x) \approx 1 + x$ and imposing the conserved moments one obtains the following system of linear equations

$$\begin{bmatrix} \langle \tilde{f}^{\text{eq}}, 1 \rangle & \langle \tilde{f}^{\text{eq}}, c_x \rangle & \langle \tilde{f}^{\text{eq}}, c_y \rangle & \langle \tilde{f}^{\text{eq}}, c_z \rangle & \langle \tilde{f}^{\text{eq}}, c^2 \rangle \\ \langle \tilde{f}^{\text{eq}}, c_x \rangle & \langle \tilde{f}^{\text{eq}}, c_x^2 \rangle & \langle \tilde{f}^{\text{eq}}, c_x c_y \rangle & \langle \tilde{f}^{\text{eq}}, c_x c_z \rangle & \langle \tilde{f}^{\text{eq}}, c^2 c_x \rangle \\ \langle \tilde{f}^{\text{eq}}, c_y \rangle & \langle \tilde{f}^{\text{eq}}, c_x c_y \rangle & \langle \tilde{f}^{\text{eq}}, c_y^2 \rangle & \langle \tilde{f}^{\text{eq}}, c_y c_z \rangle & \langle \tilde{f}^{\text{eq}}, c^2 c_y \rangle \\ \langle \tilde{f}^{\text{eq}}, c_z \rangle & \langle \tilde{f}^{\text{eq}}, c_x c_z \rangle & \langle \tilde{f}^{\text{eq}}, c_y c_z \rangle & \langle \tilde{f}^{\text{eq}}, c_z^2 \rangle & \langle \tilde{f}^{\text{eq}}, c^2 c_z \rangle \\ \langle \tilde{f}^{\text{eq}}, c^2 \rangle & \langle \tilde{f}^{\text{eq}}, c^2 c_x \rangle & \langle \tilde{f}^{\text{eq}}, c^2 c_y \rangle & \langle \tilde{f}^{\text{eq}}, c^2 c_z \rangle & \langle \tilde{f}^{\text{eq}}, c^4 \rangle \end{bmatrix} \begin{bmatrix} \hat{\mu} \\ \hat{\zeta}_x \\ \hat{\zeta}_y \\ \hat{\zeta}_z \\ \hat{\gamma} \end{bmatrix} = \begin{bmatrix} \rho - \langle \tilde{f}^{\text{eq}}, 1 \rangle \\ \rho u_x - \langle \tilde{f}^{\text{eq}}, c_x \rangle \\ \rho u_y - \langle \tilde{f}^{\text{eq}}, c_y \rangle \\ \rho u_z - \langle \tilde{f}^{\text{eq}}, c_z \rangle \\ 3\rho\theta + \rho u^2 - \langle \tilde{f}^{\text{eq}}, c^2 \rangle \end{bmatrix}. \quad (20)$$

Any linear algebra solver can be used for the above system of equations for the Lagrange multipliers $\mu, \zeta_x, \zeta_y, \zeta_z, \gamma$. However, the rate of convergence is strongly dependent on the initial guess values of the Lagrange multipliers. This is where the series form of equilibrium given below becomes useful

$$\tilde{f}_i^{\text{eq}} = \tilde{W}_i(\theta) \left[1 + \frac{u_\alpha c_{i\alpha}}{\theta} + \frac{u_\alpha u_\beta}{2\theta^2} (c_{i\alpha} c_{i\beta} - \theta \delta_{\alpha\beta}) - \frac{5}{3} \frac{u^2}{2\theta^2} \frac{\bar{R}}{2 + 5\bar{R}} (c_i^2 - 3\theta) + f_i^{(3)} \right], \quad (21)$$

where the series expansion of temperature-dependent weight $\tilde{W}_i(\theta)$ is

$$\begin{aligned} \tilde{W}_i(\theta) = \rho w_i & \left[1 + \frac{\eta}{2} (y_i - 3) + \frac{\eta^2}{8} (y_i^2 - 10y_i + 15) \right. \\ & \left. + \frac{\eta^3}{48} (y_i^3 - 21y_i^2 + 105y_i - 105) + \mathcal{O}(\eta^4) \right]. \end{aligned} \quad (22)$$

with the temperature deviation $\eta = \theta/\theta_0 - 1$. Note that the error correction term with \bar{R} will vanish for a model with 12th-order isotropy. The full expression with $f_i^{(3)}$ is given

in Appendix B where we also compare the errors of the true entropic equilibrium with its series expansion. Thus, the series expansion serves as a good initial guess for the Lagrange multipliers and also enables an analysis of the errors associated with the hydrodynamic limit.

IV. BENCHMARKS

Several challenging problems in the field of computational gasdynamics have coupled velocity and temperature dynamics with steep gradients. The complex dynamics has led to the development of a myriad of numerical methods [48]. The aim section of this section is to benchmark the RD3Q81 model for various canonical compressible flows. The first benchmark problem is the well-known Sod shock tube – a common test for the accuracy of compressible solvers. Next, we compare the solutions for two configurations of two-dimensional Riemann problems [49]. We then compare the evolution of kinetic energy and enstrophy for Taylor-Green vortex, followed by an in-depth analysis of transonic flow over an M219 cavity.

A. Sod Shock Tube

The Sod’s shock tube problem is the standard test case to check the accuracy and stability of compressible flow solvers. The existence of analytical solution of the one-dimensional Euler equations makes this problem the first test for compressible flow solvers. Here, the domain consists of an initially quiescent fluid divided into two regions L and R . The two regions, located in $x = -0.5$ to 0.0 (L) and $x = 0.0$ to 0.5 (R) respectively, are separated by an interface at $x = 0$ across which the initial conditions for density and pressure have a discontinuity. This sharp discontinuity in at the center of the domain generates a moving compressive shock front in the low density region and rarefaction front in the high density region. The two fronts leave behind in the tube a central contact region of uniform pressure and velocity [48]. The left half of the domain is initialized with a density, velocity, and

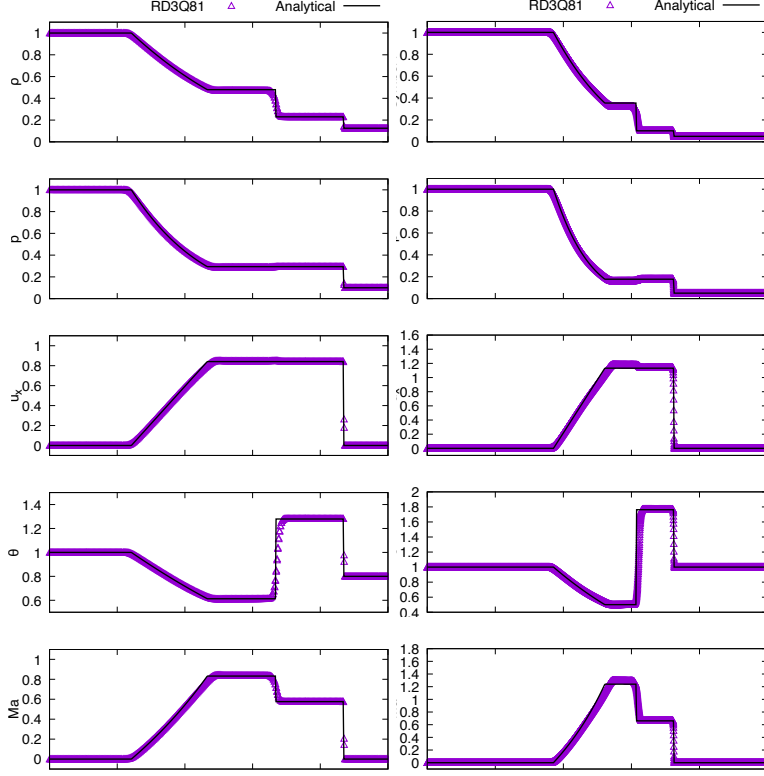


FIG. 2: Density, pressure, velocity, temperature, and Ma for Sod shock tube at a Mach number of 0.8 [left] and 1.2 [right].

pressure of $\{\rho, u, p\}_L = \{1, 0, 1\}$ while the right half is varied as

$$\begin{aligned}
 \text{IC}_1 : \{\rho, u, p\}_R &= \{0.125, 0, 0.1\}, \\
 \text{IC}_2 : \{\rho, u, p\}_R &= \{0.05, 0, 0.05\}, \\
 \text{IC}_3 : \{\rho, u, p\}_R &= \{0.0125, 0, 0.0125\}, \\
 \text{IC}_4 : \{\rho, u, p\}_R &= \{0.01, 0, 0.01\},
 \end{aligned} \tag{23}$$

Here, IC_1 is the well-known Sod shock setup while the remaining three are its extensions that lead to a higher Mach number in the domain.

We discretize the physical domain via a grid of $4000 \times 8 \times 8$ points in the three spatial directions and use the reference viscosity $\mu = 10^{-5}$. The initial relaxation time τ is computed from the relation $\mu = \tau p$, where p is p_R or p_L depending on the location of the grid point. The periodic boundary conditions were implemented in y, z -normal directions and standard bounce back in x -normal direction. The time scale is chosen based on the length of the domain and speed of sound in the right section of the domain. The simulations were run till the non-dimensional time $t^* = 0.2$, that is much earlier than either of the fronts hit the

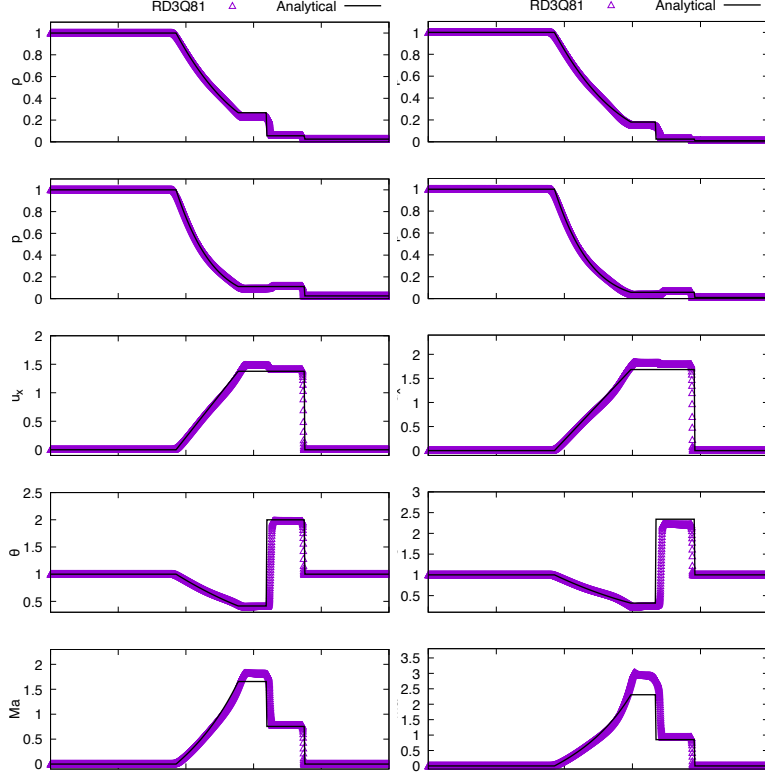


FIG. 3: Density, pressure, velocity, temperature, and Ma for Sod shock tube at a Mach number of 1.8 [left] and 2.3 [right].

wall to avoid any effect of the boundaries.

Figure 2 contrasts the density, pressure and velocity obtained from the present model with the direct integration of Navier-Stokes-Fourier equations. It is evident that the speed of the shock is captured accurately by the model for IC_1 and IC_2 . It can be seen that the model remains accurate at a Mach number of 1.3. The contact region shows a tiny departure from the vertical line which is an artifact of discretization observed in most numerical solvers. In Fig. 3, we extend the Sod shock problem with initial conditions that give rise of higher Mach numbers (IC_3 and IC_4) to test the limit of the proposed model. A small departure from analytical solution is observed at Mach number of 1.8. At Mach number 2.3, the density and pressure profiles are captured well, however, there is an appreciable deviation velocity and temperature profiles that percolates to a larger error in the predicted Mach number. It should however be noted that the model remains numerically stable till a Mach number of 3.

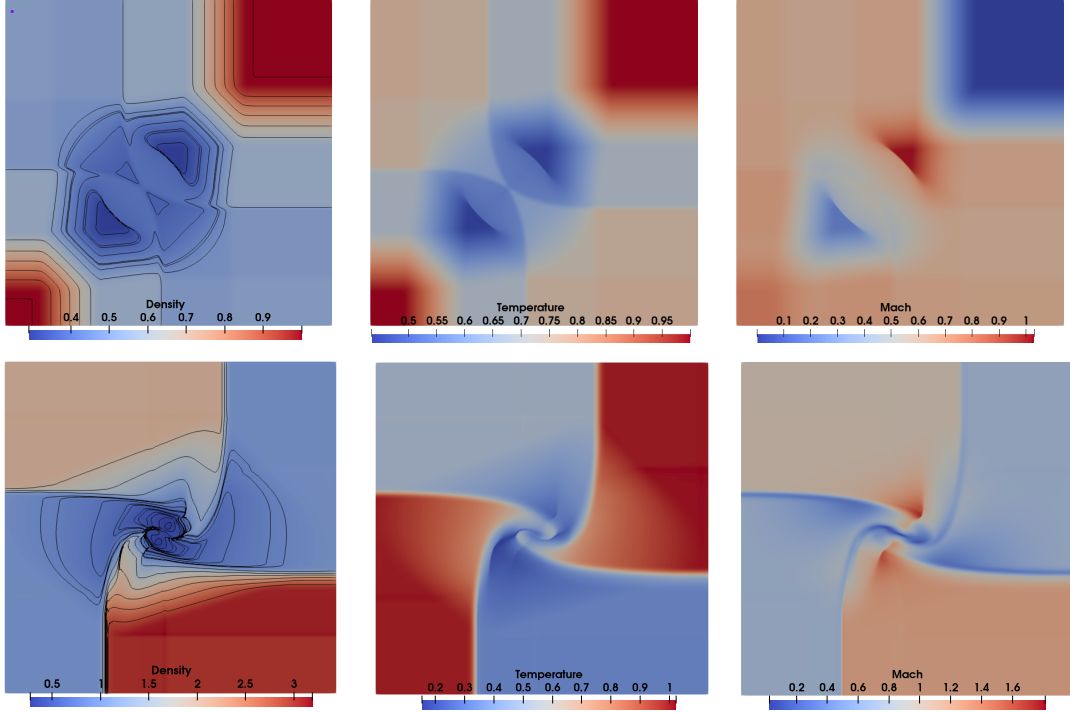


FIG. 4: Visualizations of the density, temperature, and Mach for the 2D Riemann setup: configuration II (top row) and VI (bottom row). The black solid lines represent the iso-density contours are included in the first column.

B. Two-dimensional Riemann Problem

The two-dimensional Riemann problem serves as an important benchmark for numerical methods for compressible flows [50]. Here, a square domain is decomposed into four quadrants where each quadrant is initialized with a different state. The resulting dynamics gives rise to complicated flow patterns. The initial conditions have been compiled into a set of 19 configurations [51] that have been extensively studied by hyperbolic solvers [50, 52]. We select the II and VI configurations to evaluate the accuracy of RD3Q81 model and compare with HyPar [53] – a finite-difference solver for hyperbolic-parabolic partial differential equations.

Figure 4 visualizes the density, temperature, and Mach numbers for the configuration II (top row) and VI (bottom row). The presence of shocks and steep-gradients in the domain is captured well by the RD3Q81 model. The black solid lines represent the iso-density contours are included in the first column. We perform a quantitative comparison of the density in Fig. 5. The densities along the three equidistant vertical probes are devoid of any numerical

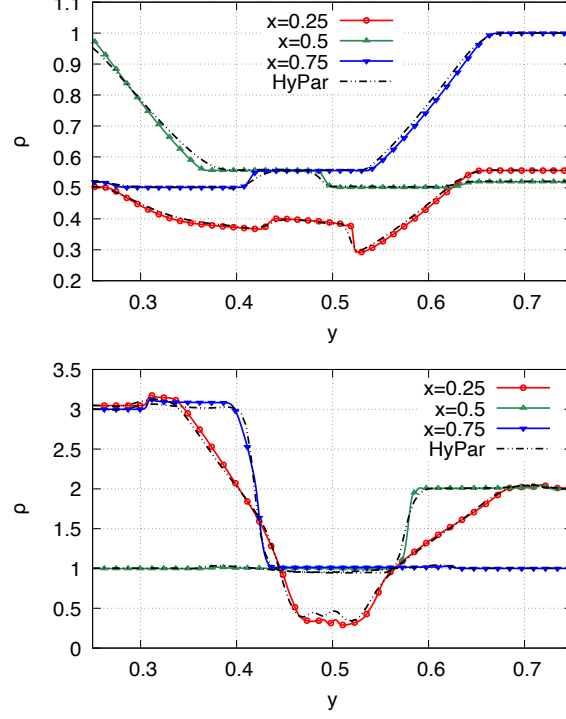


FIG. 5: The densities along the three equidistant vertical probes for 2D Riemann configurations II (top) and VI (bottom).

oscillations and exhibit an excellent match with the HyPar's output.

C. Compressible Taylor-Green Vortex

In this test case we assess the accuracy of the *RD3Q81* model to capture compressible three-dimensional turbulence accurately. The initial condition consists of eight vortices in a triply periodic domain. The dynamic is well suited to represent the geometry of evolving vortical structures under compressible conditions. The flow initially transitions to turbulence by creating small vortical structures followed by an isotropic homogeneous decay. The initial flow field is given by

$$u_1 = V_0 \sin \hat{x} \cos \hat{y} \cos \hat{z}, \quad (24)$$

$$u_2 = -V_0 \cos \hat{x} \sin \hat{y} \cos \hat{z}, \quad (25)$$

$$u_3 = 0, \quad (26)$$

$$p = p_0 + \frac{\rho_0 V_0^2}{16} [\cos 2\hat{x} + \cos 2\hat{y}] [\cos 2\hat{z} + 2], \quad (27)$$

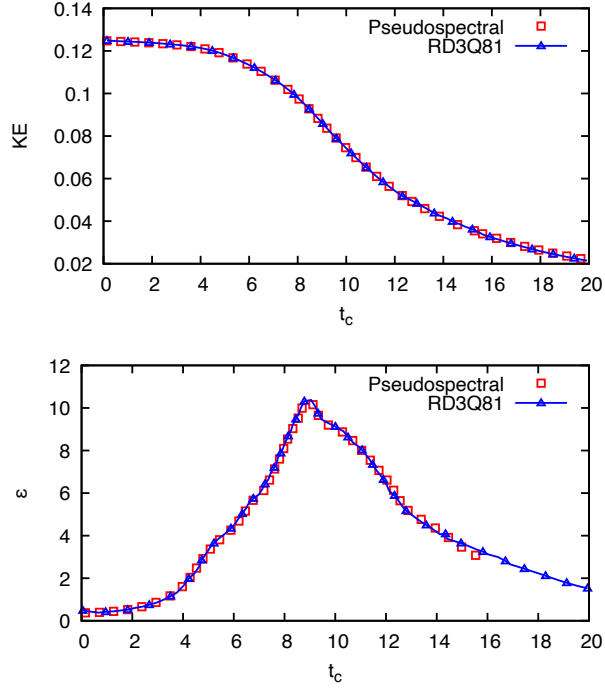


FIG. 6: Evolution of kinetic energy (top) and enstrophy (bottom) for $Ma = 0.1$ and $Re = 1600$.

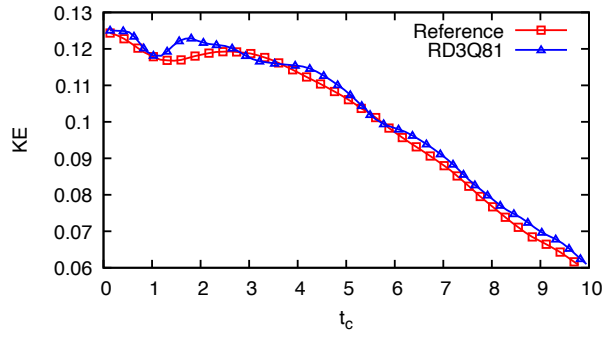


FIG. 7: Evolution of kinetic energy for $Ma = 1$ and $Re = 400$.

where $\hat{x} = x/L$, $\hat{y} = y/L$, $\hat{z} = z/L$ and pressure is consistent with the incompressibility condition. The strength of compressibility of the flow is characterized by the Mach number $Ma = V_0/c_s$ where $c_s = \sqrt{\gamma\theta_0}$ with $\gamma = 5/3$ for an ideal gas. The Reynolds number (Re) of the flow is defined by $Re = V_0L/\nu$ where $L = 2\pi$ and ν is the kinematic viscosity related to the the relaxation time τ by $\nu = \tau\theta$.

Figure 6 plots the kinetic energy and enstrophy for compressible Taylor-Green vortex simulated on a grid of 512^3 points at $Ma = 0.1, Re = 1600$. The mean turbulent kinetic

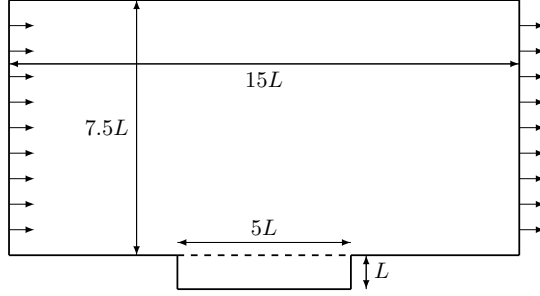


FIG. 8: Computational setup of the M219 cavity. The spanwise depth is $3L$, with the cavity placed at the center.

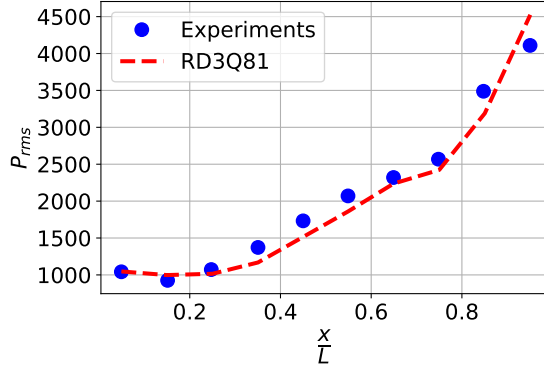


FIG. 9: Root mean square pressure on the cavity floor.

energy is computed by

$$\text{KE} = \frac{1}{\|\Omega\|} \int_{\Omega} \rho \frac{\mathbf{u} \cdot \mathbf{u}}{2} d\Omega, \quad (28)$$

where ρ is density, Ω is volume of the computational domain, and $\mathbf{u} = \{u_1, u_2, u_3\}$ is the velocity vector. The mean enstrophy ε is given by

$$\varepsilon = \frac{1}{\|\Omega\|} \int_{\Omega} \rho \frac{\omega \cdot \omega}{2} d\Omega \quad (29)$$

where $\omega = \nabla \times u$ is the vorticity. We compare the kinetic energy and enstrophy with the output of a pseudospectral solver and observe a good match. Next, we calculate the kinetic energy at a higher Mach of unity where compressibility effects are more pronounced. Figure 7 compares the kinetic energy with Ref. [54].

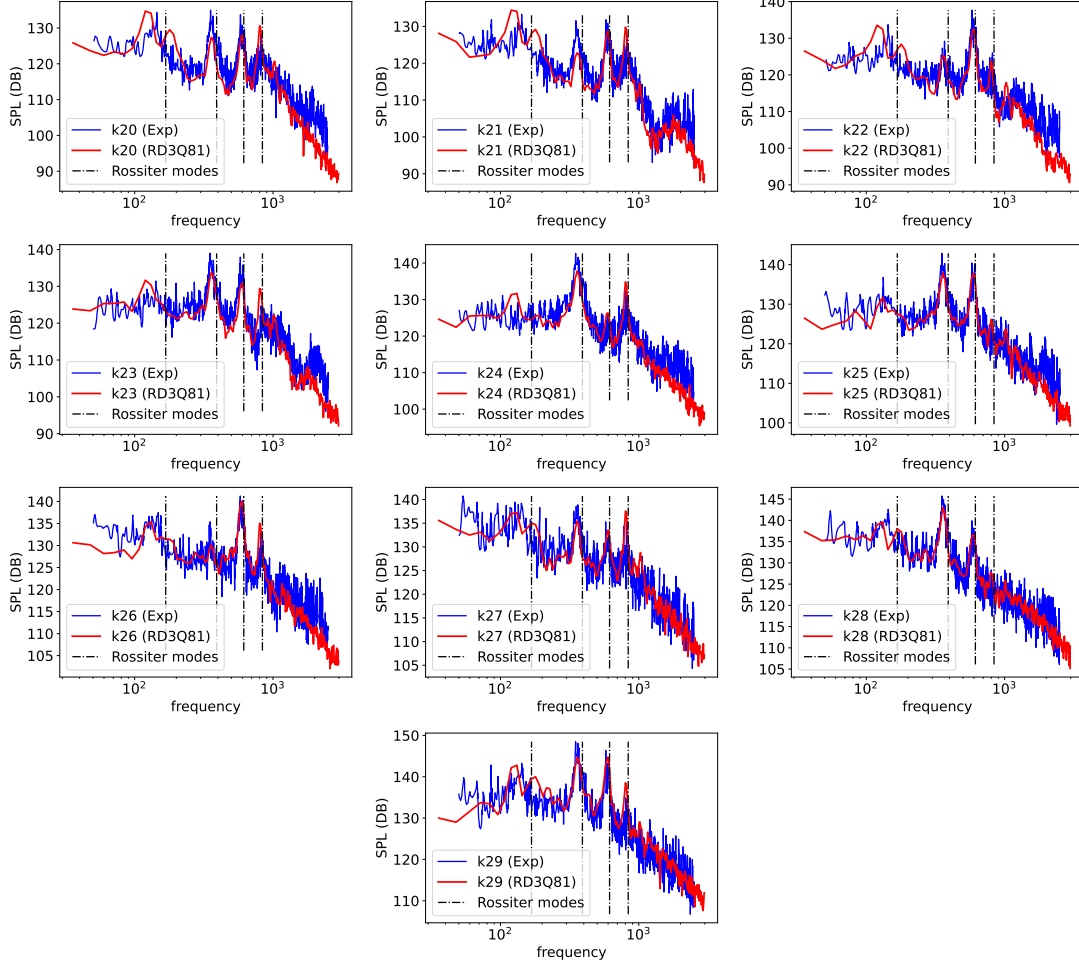


FIG. 10: Sound Pressure Level (SPL) at different probe locations ($k_{20} - k_{29}$) on the surface of the cavity

D. Aeroacoustics in a Transonic Cavity

As a final benchmark problem of high practical relevance, we analyze the aeroacoustics of M219 cavity flow in this section. The flow of open cavity finds applications in various industrial settings such as an open sunroof or a window of a vehicle, landing gear wells or the weapon bays of an aircraft. Aeroacoustic investigations are important to reduce undesirable sound and predict structural failures from self-sustaining oscillations in open cavities. These oscillations arise due to pressure waves generated from the vortical structures generated by the shear layer at the leading edge. Thus, high-fidelity simulations of cavity acoustics form indispensable tools to understanding of cavity acoustics and designing cavities. Such studies offer accurate insights into designs of cavities that lie beyond the excitation frequencies for

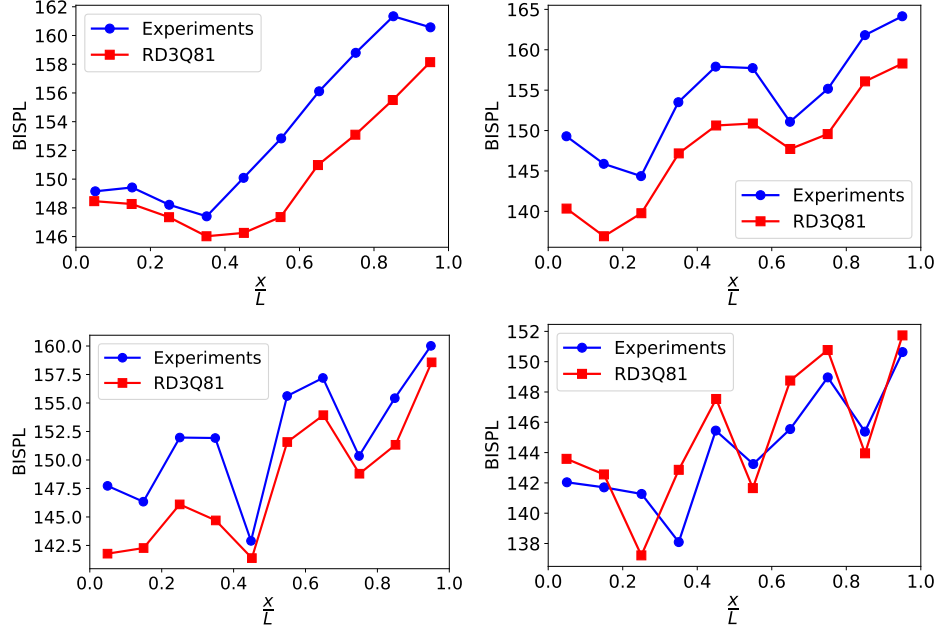


FIG. 11: Band Integrated Sound Pressure Level (BISPL) in comparison with experimental results

various flow configurations.

Figure 8 depicts the computational domain for the cavity in the current investigations. The cavity has a square cross section of height and depth L which is placed at the center of a domain of spanwise depth $3L$. The top edge of the domain is placed at a distance of $8.5L$ from the cavity floor. The length of the cavity is $5L$ placed at the center of a domain of length $15L$. Thus, both the inlet and the outlet of the computational domain are at a distance of $5L$ from the cavity's leading and trailing edges. A subsonic inlet boundary condition is specified at the inlet which is based on the total pressure and temperature. A static pressure boundary condition is applied at the outlet whereas symmetry conditions are applied at the top wall and in spanwise directions. The diffuse bounce-back boundary condition is specified at the bottom flat plate and the cavity walls [55]. The numerical simulations are carried out for $L = 0.1016\text{m}$ with a uniform mesh resolution of 0.5mm throughout the domain. The Mach number is 0.85 whereas the Reynolds number based on the cavity length is 6.7×10^6 . The inlet is maintained at a total pressure of 100969 Pa and temperature of 309 K . In the cavity experiments of Ref. [56] the pressure was measure with Kulite transducers which were placed at ten equidistant locations (represented by $k20$ to $k29$) between the leading edge and the trailing edge of the cavity.

TABLE II: Comparison of frequencies of tonal modes between experiments, simulations and Rossiter’s formula

Mode frequency (Hz)	Mode 1	Mode 2	Mode 3	Mode 4
Experiment	135	350	590	820
Modified Rossiter’s formula	167	391	614	838
RD3Q81	133	364	605	810
% error between RD3Q81 and experiments	1.4	4.0	2.5	1.2

TABLE III: Frequency bands for Rossiter modes used for computing BISPL

Rositter mode frequency (Hz)	Mode 1	Mode 2	Mode 3	Mode 4
Lower limit	50	250	500	700
Upper limit	250	450	700	900

Figure 9 plots the root mean square of pressure on the cavity floor and compares it with the various probe locations of Ref. [56]. An excellent match can be observed in the figure. Next, we compute the sound pressure level (SPL) with at the different probe locations and compare them with the experimental data. A good match is observer in Fig. 10 at all probe locations which also includes the semi-impirical tonal modes proposed by Rossiter [57]. Table II reports the tonal modes of the experiment and modified-Rossiter’s relations [58] and compares them with the RD3Q81 model’s prediction. It can be seen that the RD3Q81 model is able to accurately predict the tonal modes.

Finally, to understand the mode shapes we compute the band-integrated sound pressure level (BISPL) by integrating the frequencies for each Rossiter mode at all the probe locations. The lower and upper limits of frequencies chosen for computing BISPL are tabulated in Table III where the width of the frequency band for each mode is 200Hz. The mode shapes obtained from BISPL are shown in the Fig. 11 from where it can be seen from all the BISPL curves closely match the experimental results.

V. OUTLOOK

In this paper, we have developed a body-centered cubic lattice Boltzmann model *RD3Q81* suitable for transonic flows. We have demonstrated that the advantage of these models lies in their conceptual simplicity which is the reason for scalability of lattice Boltzmann method. We have derived the entropic equilibrium for the model and simulated several benchmark problems of theoretical and practical interest using the proposed model. This model extends the simplicity of the standard lattice Boltzmann method to flows with moderate Mach numbers where compressibility effects are dominant. We have also detailed the procedure for constructing such models which relies on imposing higher-order isotropy on the discrete velocity model and matching the trace with Maxwell-Boltzmann distribution up to the tenth order. The limitation on Mach number is shown to arise due to deviation of the trace of 12th and 14th order moments. However, the procedure can be extended to construct multispeed lattices with 135 and 157 links that impose 12th and 14th order traces respectively and are suitable for supersonic and hypersonic flows. It should be noted that the velocities and Mach numbers in the Riemann problems are positive, however, *RD3Q81* model will attain similar Mach number for the negative velocities also thus extending the range of Mach numbers for realistic applications. The *RD3Q81* model is an improvement over *RD3Q67* model in terms of temperature deviation too, thus, this model will work well for flows with large temperature variations. For several realistic applications it is important to correctly model the internal degrees of freedom and the specific heat ratio [59, 60], thus in the future we will extend the model to diatomic and polyatomic gases too.

ACKNOWLEDGMENTS

We acknowledge SankhyaSutra Labs and the National Supercomputing Mission facility (Param Yukti) at the Jawaharlal Nehru Center for Advanced Scientific Research for computational resources. SA acknowledges support via Abdul Kalam Technology Innovation National Fellowship : 4784 (INAE/SA/4784).

Appendix A: Isotropy of the Discrete Velocity Shells in LBM

In this appendix, we derive the isotropy conditions on the shells in LBM. The three kinds of shells typically used are the simple-cubic (\mathcal{S}), face-centered cubic (\mathcal{F}), and body-centered cubic (\mathcal{B}) shells are sets of discrete velocities as:

$$\begin{aligned}\mathcal{S} &: \{(\pm 1, 0, 0), (0, \pm 1, 0), (0, 0, \pm 1)\}, \\ \mathcal{F} &: \{(\pm 1, \pm 1, 0), (0, \pm 1, \pm 1), (\pm 1, 0, \pm 1)\}, \\ \mathcal{B} &: \{(\pm 1, \pm 1, \pm 1), (\pm 1, \pm 1, \pm 1)\}.\end{aligned}\tag{A1}$$

Thus, there are six links in the simple-cubic shell, twelve links in the FCC shell, and eight links in the BCC shell with the directions. These shells form the basis of all discrete velocity models typically used in LBM. The multispeed models retain the structure of shells while increasing the magnitudes by an integral factor.

1. Fourth-order isotropy

We first derive the fourth-order isotropy given in Eq. (4) for $c = 1$. A general fourth-order tensor can be described by a linear combination of isotropic fourth order Kronecker delta tensor $[\Delta_{\alpha\beta\gamma\kappa} = \delta_{\alpha\beta}\delta_{\gamma\kappa} + \delta_{\alpha\gamma}\delta_{\beta\kappa} + \delta_{\beta\gamma}\delta_{\alpha\kappa}]$ and anisotropic fourth-order tensor $[\delta_{\alpha\beta\gamma\kappa}]$. Thus, for each shell $\mathcal{S}, \mathcal{F}, \mathcal{B}$ one writes fourth-order tensors representing moments of discrete velocities as

$$\begin{aligned}\sum_{i \in \mathcal{S}} \frac{c_{i\alpha} c_{i\beta} c_{i\gamma} c_{i\kappa}}{c^4} &= a_1 \delta_{\alpha\beta\gamma\kappa} + a_2 \Delta_{\alpha\beta\gamma\kappa}, \\ \sum_{i \in \mathcal{F}} \frac{c_{i\alpha} c_{i\beta} c_{i\gamma} c_{i\kappa}}{c^4} &= a_3 \delta_{\alpha\beta\gamma\kappa} + a_4 \Delta_{\alpha\beta\gamma\kappa}, \\ \sum_{i \in \mathcal{B}} \frac{c_{i\alpha} c_{i\beta} c_{i\gamma} c_{i\kappa}}{c^4} &= a_5 \delta_{\alpha\beta\gamma\kappa} + a_6 \Delta_{\alpha\beta\gamma\kappa}.\end{aligned}\tag{A2}$$

Now, we substitute for $c = 1$ and $\alpha = \beta = \gamma = \kappa = x$ in Eq. (A2) to obtain

$$\begin{aligned}\sum_{i \in \mathcal{S}} c_{ix}^4 &= 2 = a_1 + 3a_2, \\ \sum_{i \in \mathcal{F}} c_{ix}^4 &= 8 = a_3 + 3a_4, \\ \sum_{i \in \mathcal{B}} c_{ix}^4 &= 8 = a_5 + 3a_6.\end{aligned}\tag{A3}$$

and $\alpha = \beta = x, \gamma = \kappa = y$ in Eq. (A2) to obtain

$$\begin{aligned}\sum_{i \in \mathcal{S}} c_{ix}^2 c_{iy}^2 &= 0 = a_2, \\ \sum_{i \in \mathcal{F}} c_{ix}^2 c_{iy}^2 &= 4 = a_4, \\ \sum_{i \in \mathcal{B}} c_{ix}^2 c_{iy}^2 &= 8 = a_6.\end{aligned}\tag{A4}$$

The system of equations (A3) – (A4) are solved to obtain the coefficients of isotropic and anisotropic components of fourth order moments of discrete velocity set.

2. Sixth-order isotropy

Next, we derive the sixth-order isotropy given in Eq. (5) for $c = 1$. Similar to the procedure in the previous section, we write a generic sixth-order tensor as a linear combination of isotropic tensor $\Delta_{\alpha\beta\gamma\kappa\eta\zeta}$ and anisotropic tensors $\delta_{\alpha\beta\gamma\kappa\eta\zeta}$ and $\delta_{\alpha\beta\gamma\kappa\eta\zeta}^{(4,2)}$. Thus, for each shell one writes sixth-order tensors representing moments of discrete velocities as

$$\begin{aligned}\sum_{i \in \text{SC}} \frac{c_{i\alpha} c_{i\beta} c_{i\gamma} c_{i\kappa} c_{i\eta} c_{i\zeta}}{c^6} &= a_1 \delta_{\alpha\beta\gamma\kappa\eta\zeta} + a_2 \delta_{\alpha\beta\gamma\kappa\eta\zeta}^{(4,2)} + a_3 \Delta_{\alpha\beta\gamma\kappa\eta\zeta}, \\ \sum_{i \in \text{FCC}} \frac{c_{i\alpha} c_{i\beta} c_{i\gamma} c_{i\kappa} c_{i\eta} c_{i\zeta}}{c^6} &= a_4 \delta_{\alpha\beta\gamma\kappa\eta\zeta} + a_5 \delta_{\alpha\beta\gamma\kappa\eta\zeta}^{(4,2)} + a_6 \Delta_{\alpha\beta\gamma\kappa\eta\zeta}, \\ \sum_{i \in \text{BCC}} \frac{c_{i\alpha} c_{i\beta} c_{i\gamma} c_{i\kappa} c_{i\eta} c_{i\zeta}}{c^6} &= a_7 \delta_{\alpha\beta\gamma\kappa\eta\zeta} + a_8 \delta_{\alpha\beta\gamma\kappa\eta\zeta}^{(4,2)} + a_9 \Delta_{\alpha\beta\gamma\kappa\eta\zeta}.\end{aligned}\tag{A5}$$

Now, we first substitute $c = 1$ and $\alpha = \beta = \gamma = \kappa = \eta = \zeta = x$ in Eq. (A5)

$$\begin{aligned}\sum_{i \in \text{SC}} c_{ix}^6 &= 2 = a_1 + 15a_2 + 15a_3 \\ \sum_{i \in \text{FCC}} c_{ix}^6 &= 8 = a_4 + 15a_5 + 15a_6 \\ \sum_{i \in \text{BCC}} c_{ix}^6 &= 8 = a_7 + 15a_8 + 15a_9,\end{aligned}\tag{A6}$$

followed by $\alpha = \beta = \gamma = \kappa = x$ and $\eta = \zeta = y$ in Eq. (A5)

$$\begin{aligned}\sum_{i \in \text{SC}} c_{ix}^6 &= 0 = a_2 + 3a_3 \\ \sum_{i \in \text{FCC}} c_{ix}^6 &= 4 = a_5 + 3a_6 \\ \sum_{i \in \text{BCC}} c_{ix}^6 &= 8 = a_8 + 3a_9,\end{aligned}\tag{A7}$$

Discrete velocity	$D3Q15$	$D3Q19$	$D3Q27$	$D3Q41$
θ_0	1/3	1/3	1/3	$1 - \sqrt{2/5}$
$(\pm 1, 0, 0), (0, \pm 1, 0), (0, 0, \pm 1)$	1/9	1/18	2/27	$37/(5\sqrt{10}) - 91/40$
$(\pm 1, \pm 1, 0), (\pm 1, 0, \pm 1), (0, \pm 1, \pm 1)$	-	1/36	1/54	$(55 - 17\sqrt{10})/50$
$(\pm 1, \pm 1, \pm 1)$	1/72	-	1/216	$(233\sqrt{10} - 730)/1600$
$(\pm 3, 0, 0), (0, \pm 3, 0), (0, 0, \pm 3)$	-	-	-	$(295 - 92\sqrt{10})/16200$
$(\pm 3, \pm 3, \pm 3)$	-	-	-	$(130 - 41\sqrt{10})/129600$

TABLE IV: Weights corresponding to discrete velocities for the basic LB models at the base temperature θ_0 .

Shells	Discrete Velocities(c_i/c)	Weights [$w_i = W(\theta = \theta_0)$]
SC-1	$(\pm 1, 0, 0), (0, \pm 1, 0), (0, 0, \pm 1)$	$(388800\theta_0 - 2508408\theta_0^2 + 7033852\theta_0^3 - 7856469\theta_0^4 + 2838528\theta_0^5)/486000$
SC-2	$2(\pm 1, 0, 0), 2(0, \pm 1, 0), 2(0, 0, \pm 1)$	$(-388800\theta_0 + 3091608\theta_0^2 - 8269102\theta_0^3 + 8694819\theta_0^4 - 2838528\theta_0^5)/3888000$
SC-3	$3(\pm 1, 0, 0), 3(0, \pm 1, 0), 3(0, 0, \pm 1)$	$(388800\theta_0 - 3199608\theta_0^2 + 8977852\theta_0^3 - 9120069\theta_0^4 + 2838528\theta_0^5)/30618000$
SC-4	$4(\pm 1, 0, 0), 4(0, \pm 1, 0), 4(0, 0, \pm 1)$	$(-97200\theta_0 + 809352\theta_0^2 - 2315338\theta_0^3 + 2396961\theta_0^4 - 709632\theta_0^5)/108864000$
FCC-1	$(\pm 1, \pm 1, 0), (\pm 1, 0, \pm 1), (0, \pm 1, \pm 1)$	$(8\theta_0^3 - 9\theta_0^4)/(12)$
FCC-2	$2(\pm 1, \pm 1, 0), 2(\pm 1, 0, \pm 1), 2(0, \pm 1, \pm 1)$	$(-2\theta_0^3 + 9\theta_0^4)/768$
BCC-1/2	$(\pm 0.5, \pm 0.5, \pm 0.5)$	$(24300\theta_0^2 - 103834\theta_0^3 + 126963\theta_0^4 - 44352\theta_0^5)/7776$
BCC -1	$(\pm 1.0, \pm 1.0, \pm 1.0)$	$(-24300\theta_0^2 + 189022\theta_0^3 - 328275\theta_0^4 + 177408\theta_0^5)/272160$
BCC -3/2	$(\pm 1.5, \pm 1.5, \pm 1.5)$	$(2700\theta_0^2 - 24778\theta_0^3 + 67995\theta_0^4 - 44352\theta_0^5)/699840$
BCC -5/2	$(\pm 2.5, \pm 2.5, \pm 2.5)$	$(-972\theta_0^2 + 11818\theta_0^3 - 43371\theta_0^4 + 44352\theta_0^5)/68040000$

TABLE V: Energy shells and their corresponding velocities with weights w_i for $RD3Q81$ with $\theta_0 = 0.821035006329447750282591763$.

and finally $\alpha = \beta = x, \gamma = \kappa = y, \eta = \zeta = x$ in Eq. (A5)

$$\begin{aligned}
\sum_{i \in \text{SC}} c_{ix}^6 &= 0 = a_3 \\
\sum_{i \in \text{FCC}} c_{ix}^6 &= 0 = a_5 \\
\sum_{i \in \text{BCC}} c_{ix}^6 &= 8 = a_9,
\end{aligned} \tag{A8}$$

The system of equations (A6) – (A8) are solved to obtain the coefficients of isotropic and anisotropic components of sixth order moments of discrete velocity set.

Moments	D3Q15	D3Q19	D3Q27	D3Q41	D3Q125	RD3Q41	RD3Q67	RD3Q81
θ_0	1/3	1/3	1/3	$1 - \sqrt{2/5}$	$1 - \sqrt{2/5}$	0.29...	0.74...	0.82...
$\mathcal{O}(c^4)$								
$\langle w, c^2 c_x^2 \rangle$	0%	0%	0%	0%	0%	0%	0%	0%
$\langle w, c_x^2 c_y^2 \rangle$	Imposed	Imposed	Imposed	Imposed	Imposed	Imposed	Imposed	Imposed
$\langle w, c_x^4 \rangle$	Imposed	Imposed	Imposed	Imposed	Imposed	Imposed	Imposed	Imposed
$\mathcal{O}(c^6)$								
$\langle w, c^4 c_x^2 \rangle$	-5.7%	-22%	-17%	0%	0%	Imposed	0%	0%
$\langle w, c^2 c_x^4 \rangle$	-28%	-28%	-28%	0%	0%	Imposed	0%	0%
$\langle w, c^2 c_x^2 c_y^2 \rangle$	-28%	-14%	0%	0%	0%	Imposed	0%	0%
$\langle w, c_x^2 c_y^2 c_z^2 \rangle$	200%	-100%	Imposed	Imposed	Imposed	65%	Imposed	Imposed
$\langle w, c_x^4 c_y^2 \rangle$	0%	0%	0%	Imposed	Imposed	10%	Imposed	Imposed
$\langle w, c_x^6 \rangle$	40%	-40%	-40%	Imposed	Imposed	4.3%	Imposed	Imposed
$\mathcal{O}(c^8)$								
$\langle w, c^6 c_x^2 \rangle$	-17%	-51%	-40%	69%	32%	Imposed	Imposed	0%
$\langle w, c^4 c_x^4 \rangle$	-47%	-57%	-53%	67%	54%	4.4%	Imposed	0%
$\langle w, c^4 c_x^2 c_y^2 \rangle$	28%	-42%	-19%	71%	0%	-6.6%	Imposed	0%
$\langle w, c^2 c_x^2 c_y^2 c_z^2 \rangle$	200%	-100%	0%	218%	0%	66%	40%	Imposed
$\langle w, c^2 c_x^4 c_y^2 \rangle$	0%	-33%	-22%	46%	0%	-18%	6.7%	Imposed
$\langle w, c^2 c_x^6 \rangle$	-66%	-66%	-66%	76%	76%	13%	2.7%	Imposed
$\langle w, c_x^4 c_y^2 c_z^2 \rangle$	200%	-100%	0%	218%	Imposed	66%	40%	0%
$\langle w, c_x^4 c_y^2 c_z^2 \rangle$	0%	0%	0%	66%	Imposed	-6.1%	50%	33.33%
$\langle w, c_x^6 c_y^2 \rangle$	-40%	-40%	-40%	0%	Imposed	-43%	9.7%	-19.99%
$\langle w, c_x^8 \rangle$	-74%	-74%	-74%	98%	98%	30%	0.70%	5.7%
$\mathcal{O}(c^{10})$								
$\langle w, c^8 c_x^2 \rangle$	-35.32%	-74.28%	-61.29%	494%	137.1%	-5.59%	Imposed	0%
$\langle w, c^6 c_x^4 \rangle$	-62.33%	-77.92%	-72.72%	376%	208%	5.59%	-1.18%	Imposed
$\langle w, c^6 c_x^2 c_y^2 \rangle$	5.19%	-68.83%	-44.15%	670%	29.79%	-22.38%	1.78%	Imposed
$\langle w, c^4 c_x^2 c_y^2 c_z^2 \rangle$	145.4%	-100%	-18.18%	1658%	0%	49.64%	-66.41%	17.66%
$\langle w, c^4 c_x^4 c_y^2 \rangle$	-18.18%	-63.63%	-48.48%	506%	34.76%	34.38%	13.14%	-2.94%
$\langle w, c^4 c_x^6 \rangle$	-80%	-83.63%	-82.42%	324%	278%	21.59%	-6.91%	1.17%
$\langle w, c^2 c_x^4 c_y^2 c_z^2 \rangle$	145.4%	-100%	-18.18%	1658%	0%	49.64%	66.41%	17.66%
$\langle w, c^2 c_x^4 c_y^4 \rangle$	-18.18%	-45.45%	-36.36%	516%	0%	-26.52%	64.12%	25.97%
$\langle w, c^2 c_x^6 c_y^2 \rangle$	-50.90%	-67.27%	61.81%	269%	62.57%	-55.91%	-1.52%	-24.41%
$\langle w, c^2 c_x^8 \rangle$	-88.31%	-88.31%	-88.31%	3400%	3400%	43.73%	-8.45%	8.49%
$\langle w, c_x^{10} \rangle$	-91.42%	-91.42%	-91.42%	393%	393%	69.71%	-4.91%	20.77%
$\langle w, c_x^8 c_y^2 \rangle$	-74.28%	-74.28%	-74.28%	98.32%	98.32%	-73.20%	-24.38%	-46.77%
$\langle w, c_x^6 c_y^4 \rangle$	-40%	-40%	-40%	362%	Imposed	-37.46%	76.42%	24.18%
$\langle w, c_x^6 c_y^2 c_z^2 \rangle$	80%	-100%	-40%	1189%	Imposed	9.73%	-75.37%	-13.71%
$\langle w, c_x^4 c_y^4 c_z^2 \rangle$	200%	-100%	0%	2049%	Imposed	82.89%	-58.95%	43.81%

TABLE VI: Percentage errors in the various moments [$\mathcal{O}(c^4)$ to $\mathcal{O}(c^{10})$] of various lattice Boltzmann models. To construct models that remain accurate at higher Mach numbers the errors in the higher moments should be reduced without impacting the lower moments.

Appendix B: Series expansion of discrete entropic equilibrium

In this section, we first construct the series expansion of temperature-dependent weights at an arbitrary temperature θ and then extend it to nonzero velocity equilibrium.

1. Temperature-dependent weights

Let the weights of the shells at $\theta = \theta_0$ be $w_{\text{SC1}}, w_{\text{SC2}}, w_{\text{SC3}}, w_{\text{SC4}}, w_{\text{FCC1}}, w_{\text{FCC2}}, w_{\text{BCCH}}, w_{\text{BCC1}}, w_{\text{BCC3H}},$ and w_{BCC5H} . We need to find weights as a functions of temperature as $W(\theta)$ [32], such that

$$1 = \langle W(\theta), \tilde{1} \rangle, \quad 0 = \langle W(\theta), c_\alpha \rangle, \quad 3\theta = \langle W(\theta), c^2 \rangle. \quad (\text{B1})$$

Formally, we can write the temperature-dependent weight as

$$W(\theta) = w_i \exp(\mu^{(0)} + \zeta_\kappa^{(0)} c_\kappa + \gamma^{(0)} c_i^2) \equiv w_i A G^{4c_i^2} \quad (\text{B2})$$

where $\zeta_\kappa^{(0)} = 0$ and $A = \exp \mu^{(0)}$ and $G = \exp(\gamma^{(0)} c^2/4)$. Imposing mass and energy conservation one obtains

$$\begin{aligned} \langle w_i G^{4c_i^2/c^2}, \tilde{1} \rangle &\equiv F_0(G) = \frac{1}{A} \quad \text{and} \\ \langle w_i G^{4c_i^2}, c_i^2 \rangle &\equiv F_2(G) = \frac{3\theta'\theta_0}{A}, \end{aligned} \quad (\text{B3})$$

where $\theta' = \theta/\theta_0$, and $F_0(G), F_2(G)$ are respectively expanded as

$$\begin{aligned} F_0(G) &= w_0 + 6w_{\text{SC1}}G^4 + 6w_{\text{SC2}}G^{16} + 6w_{\text{SC3}}G^{36} \\ &+ 6w_{\text{SC4}}G^{64} + 12w_{\text{FCC1}}G^8 + 12w_{\text{FCC2}}G^{32} + 8w_{\text{BCCH}}G^3 \\ &+ 8w_{\text{BCC1}}G^{12} + 8w_{\text{BCC3H}}G^{27} + 8w_{\text{BCC5H}}G^{75}, \\ F_2(G) &= 6w_{\text{SC1}}G^4 + 24w_{\text{SC2}}G^{16} + 54w_{\text{SC3}}G^{36} \\ &+ 96w_{\text{SC4}}G^{64} + 24w_{\text{FCC1}}G^8 + 96w_{\text{FCC2}}G^{32} + 6w_{\text{BCCH}}G^3 \\ &+ 24w_{\text{BCC1}}G^{12} + 54w_{\text{BCC3H}}G^{27} + 150w_{\text{BCC5H}}G^{75}. \end{aligned} \quad (\text{B4})$$

Simplifying Eq. (B4), one obtains

$$\theta'(G) = \frac{F_2(G)}{3\theta_0 F_0(G)}. \quad (\text{B5})$$

The above equation is highly nonlinear in G which represents the relationship between the temperature θ and its associated Lagrange multiplier (see Fig. 12). In practice, the

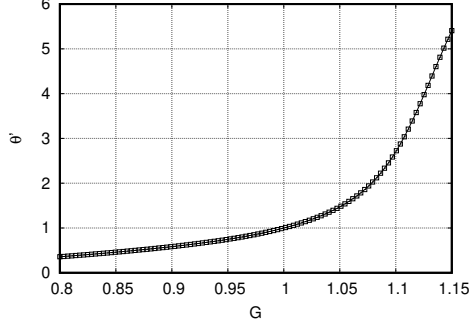


FIG. 12: The relationship between the temperature θ and its associated Lagrange multiplier.

temperature θ at each point is known and G corresponding to it needs to be calculated. This can be accomplished with any iterative numerical solver or by writing a series expansion in the temperature deviation $\eta = \theta/\theta_0 - 1$.

To construct the series expansion $\tilde{W}(\theta)$, we write a perturbation series of $W(\theta)$ [Eq. (B2)] in η around the reference state $\theta = \theta_0$. We expand the Lagrange multipliers $\mu^{(0)}, \gamma^{(0)}$ as

$$\begin{aligned}\mu^{(0)} &= \mu^{(0,0)} + \eta\mu^{(0,1)} + \eta^2\mu^{(0,2)} + \dots, \\ \gamma^{(0)} &= \gamma^{(0,0)} + \eta\gamma^{(0,1)} + \eta^2\gamma^{(0,2)} + \dots.\end{aligned}\tag{B6}$$

Substituting the above expansions in Eq. (B2) one obtains

$$\tilde{W}(\theta) = w_i \exp \left[\sum_{k=0}^{\infty} \eta^k (\mu^{(0,k)} + \gamma^{(0,k)} c_i^2) \right].\tag{B7}$$

Thereafter, using the approximation $\exp(x) = 1 + x + x^2/2 + \dots$ on the above expression one obtains

$$\tilde{W}(\theta) = w_i \left[1 + W^{(0,0)} + \eta W^{(0,1)} + \dots \right]\tag{B8}$$

where

$$W^{(0,0)} = \mu^{(0,0)} + \gamma^{(0,0)} c_i^2 + \frac{1}{2} (\mu^{(0,0)} + \gamma^{(0,0)} c_i^2)^2,\tag{B9}$$

and

$$\begin{aligned}W^{(0,1)} &= \mu^{(0,1)} + \gamma^{(0,1)} c_i^2 + (\mu^{(0,0)} + \gamma^{(0,0)} c_i^2) \times \\ &\quad (\mu^{(0,1)} + \gamma^{(0,1)} c_i^2).\end{aligned}\tag{B10}$$

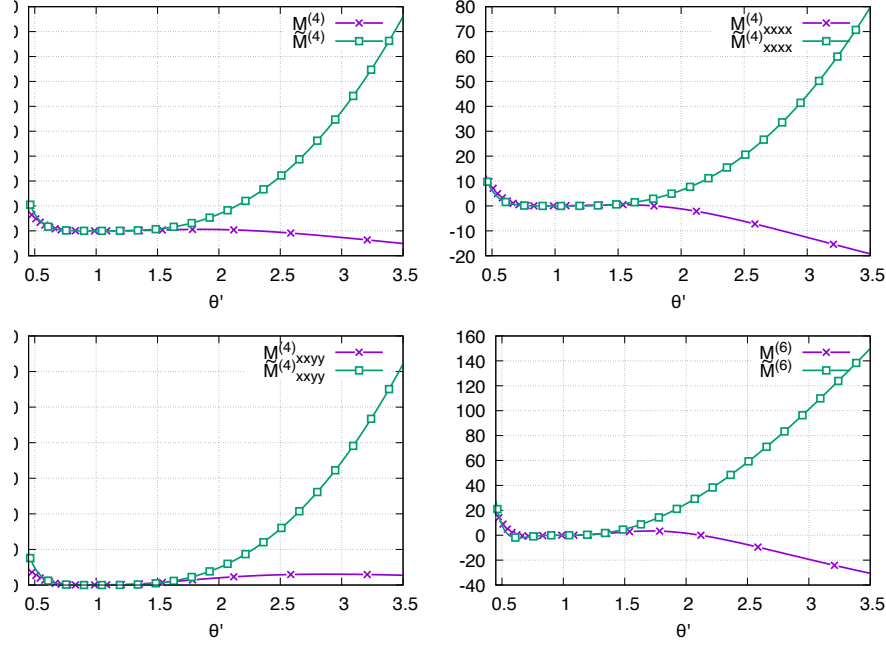


FIG. 13: Percentage error in moments of temperature-dependent weights [Eq. (B2)] and its series expansion [Eq. (B15)].

The conserved moments for $\tilde{W}(\theta)$ are

$$\left\langle \tilde{W}(\theta), \left\{ 1, \frac{c^2}{2} \right\} \right\rangle = \{1, 3\theta_0(1 + \eta)\}. \quad (\text{B11})$$

Now, matching the above two moments at various orders of η one finds the expressions for the Lagrange multipliers $\mu^{(0,k)}, \gamma^{(0,k)}$. For example, at $\mathcal{O}(1)$ one obtains $\mu^{(0,0)} = \gamma^{(0,0)} = 0$, which is trivial to see as the $\mathcal{O}(1)$ moments are satisfied by the weight w_i . Similarly, at $\mathcal{O}(\eta)$ one solves

$$\left\langle W^{(0,1)}, \left\{ 1, \frac{c^2}{2} \right\} \right\rangle = \{0, 3\theta_0\eta\}. \quad (\text{B12})$$

to obtain

$$\mu^{(0,1)} = -\frac{3}{2}, \quad \gamma^{(0,1)} = \frac{1}{2\theta_0}. \quad (\text{B13})$$

The final solution reads as

$$\begin{aligned} \mu^{(0)} &= -\frac{3}{2}\eta + \frac{6}{8}\eta^2 - \frac{1}{2}\eta^3 + \dots, \\ \gamma^{(0)} &= \frac{\eta}{2\theta_0} - \frac{\eta^2}{2\theta_0} + \frac{\eta^3}{2\theta_0} + \dots. \end{aligned} \quad (\text{B14})$$

Thus, a quartic expression for temperature-dependent weights $\tilde{W}(\theta)$ in terms of $y_i = c_i^2/\theta_0$

is obtained as

$$\begin{aligned}\tilde{W}_i(\theta) = \rho w_i & \left[1 + \frac{\eta}{2} (y_i - 3) + \frac{\eta^2}{8} (y_i^2 - 10y_i + 15) \right. \\ & + \frac{\eta^3}{48} (y_i^3 - 21y_i^2 + 105y_i - 105) \\ & \left. + \frac{\eta^4}{384} (y_i^4 - 36y_i^3 + 378y_i^2 - 1260y_i + 945) \right].\end{aligned}\tag{B15}$$

The above expansion is accurate when θ is close to the base temperature θ_0 . The deviation of the moments of the series expansion $\tilde{W}(\theta)$ deviate from the Maxwell-Boltzmann moments at a faster rate than the moments of $W(\theta)$. The practical challenge is to evaluate the Lagrange multiplier G corresponding to the local temperature with maximum accuracy. This can of course be accomplished by an iterative procedure, however, this approach results in an increased computational cost. Therefore, the choice of the initial guess to the iterative solver is important.

In Fig. 13 we plot the errors $[(M/M^{\text{MB}} - 1) \times 100]$ in fourth-order moments and the trace of the sixth-order moments for the equilibrium given by $\tilde{W}(\theta)$ and $W(\theta)$. The moments are defined as

$$\begin{aligned}M^{(4)} &= \langle W(\theta), c^2 c^2 \rangle, \tilde{M}^{(4)} = \langle \tilde{W}(\theta), c^2 c^2 \rangle, \\ M_{xxxx}^{(4)} &= \langle W(\theta), c^2 c^2 \rangle, \tilde{M}_{xxxx}^{(4)} = \langle \tilde{W}(\theta), c_x^2 c_x^2 \rangle, \\ M_{xxyy}^{(4)} &= \langle W(\theta), c_x^2 c_y^2 \rangle, \tilde{M}_{xxyy}^{(4)} = \langle \tilde{W}(\theta), c_x^2 c_y^2 \rangle, \\ M^{(6)} &= \langle W(\theta), c^2 c^2 c^2 \rangle, \tilde{M}^{(6)} = \langle \tilde{W}(\theta), c^2 c^2 c^2 \rangle, \\ M^{(4)\text{MB}} &= 15\rho\theta^2, M_{xxxx}^{(4)\text{MB}} = 3\rho\theta^2, M_{xxyy}^{(4)\text{MB}} = \rho\theta^2, \\ &M^{(6)\text{MB}} = 105\rho\theta^3.\end{aligned}\tag{B16}$$

The above moments are the ones that contribute to the errors at the leading order. It is evident that the moments of the series expansion exhibit faster growth in errors, thus it is important to use $W(\theta)$ evaluated with an iterative numerical procedure for practical applications.

2. Discrete equilibrium at nonzero velocity

We next derive the full discrete equilibrium distribution at nonzero velocity [Eq. (18)] by expanding the Lagrange multipliers in ϵ (representing smallness parameter Mach number)

as

$$\begin{aligned}\mu &= \mu^{(0)} + \epsilon \mu^{(1)} + \epsilon^2 \mu^{(2)} + \dots, \\ \zeta_\kappa &= \zeta_\kappa^{(0)} + \epsilon \zeta_\kappa^{(1)} + \epsilon^2 \zeta_\kappa^{(2)} + \dots, \\ \gamma &= \gamma^{(0)} + \epsilon \gamma^{(1)} + \epsilon^2 \gamma^{(2)} + \dots,\end{aligned}\tag{B17}$$

where $\mu^{(0)}, \zeta_\kappa^{(0)}, \gamma^{(0)}$ are the Lagrange multipliers at zero velocity as discussed in the previous section. Thus, we have

$$f_i^{\text{eq}} = W_i(\theta) \exp \left[\sum_{k=1}^{\infty} \epsilon^k Z^{(k)} \right],\tag{B18}$$

where $Z^{(k)} = \mu^{(k)} + \zeta_\kappa^{(k)} c_{i\kappa} + \gamma^{(k)} c_i^2$. We again use the approximation $\exp(x) = 1 + x + x^2/2 + \dots$ on the above expression to obtain a series expansion of the equilibrium as

$$\tilde{f}_i^{\text{eq}} = \tilde{W}_i(\theta) \left[1 + \epsilon f_i^{(1)} + \epsilon^2 f_i^{(2)} + \epsilon^3 f_i^{(3)} + \dots \right],\tag{B19}$$

where $f_i^{(0)}$ is the zero velocity equilibrium and

$$\begin{aligned}f_i^{(1)} &= Z^{(1)}, \quad f_i^{(2)} = Z^{(2)} + \frac{1}{2} [Z^{(1)}]^2, \\ f_i^{(3)} &= Z^{(3)} + Z^{(1)} Z^{(2)} + \frac{1}{6} [Z^{(1)}]^3.\end{aligned}\tag{B20}$$

The mass, momentum, and energy conservation constraints for the discrete equilibrium at any velocity can be written as

$$\left\langle \tilde{f}_i^{\text{eq}}, \left\{ 1, c_\alpha, \frac{c^2}{2} \right\} \right\rangle = \{ \rho, \epsilon u_\alpha, \epsilon^2 \rho u^2 + 3\rho\theta \}.\tag{B21}$$

The above three conditions are compared at various orders of ϵ to reveal the discrete equilibrium accurate up to $\mathcal{O}(\epsilon^3 \eta^4)$ as

$$\tilde{f}_i^{\text{eq}} = \tilde{W}_i(\theta) \left[1 + \frac{u_\alpha c_{i\alpha}}{\theta} + f_i^{(2)} + f_i^{(3)} \right],\tag{B22}$$

where

$$f_i^{(2)} = \frac{u_\alpha u_\beta}{2\theta^2} (c_{i\alpha} c_{i\beta} - \theta \delta_{\alpha\beta}) - \frac{5}{3} \frac{u^2}{2\theta^2} \frac{\bar{R}}{2 + 5\bar{R}} (c_i^2 - 3\theta),\tag{B23}$$

$$\begin{aligned}f_i^{(3)} &= \frac{u_\alpha u_\beta u_\gamma}{6\theta^3} (c_{i\alpha} c_{i\beta} c_{i\gamma} - \theta c_{i\kappa} \Delta_{\alpha\beta\gamma\kappa}) \\ &\quad - \left[\frac{5}{6\theta^3} \frac{\bar{R} u^2}{2 + 5\bar{R}} \right] u_\kappa c_{i\kappa} (c_i^2 - 3\theta) \\ &\quad + \frac{1}{6\theta^2} (5u_\chi c_{i\chi} u^2 \bar{R} - u_\alpha u_\zeta u_\eta c_{i\chi} \bar{R}_{\chi\alpha\zeta\eta}),\end{aligned}\tag{B24}$$

with

$$\bar{R}_{\kappa\alpha\zeta\eta} = \frac{1}{\theta^2} \left\langle \tilde{W}_i(\theta), c_{i\kappa} c_{i\alpha} c_{i\zeta} c_{i\eta} \right\rangle - \Delta_{\alpha\kappa\eta\zeta} \quad (\text{B25})$$

$$\text{and} \quad \bar{R} = \frac{1}{15\theta^2} \left\langle \tilde{W}_i(\theta), c_i^2 c_i^2 \right\rangle - 1. \quad (\text{B26})$$

The above equations combined with Eq. B15 provide a series expansion of the entropic equilibrium at low velocity and temperature deviation. It should also be noted that \bar{R} will vanish for a lattice that has the trace at twelfth order imposed.

-
- [1] Y. H. Qian, D. d’Humières, and P. Lallemand, *Europhys. Lett.* **17**, 479 (1992).
 - [2] H. Chen, S. Chen, and W. H. Matthaeus, *Phys. Rev. A* **45**, R5339 (1992).
 - [3] S. Chen and G. D. Doolen, *Annu. Rev. Fluid Mech.* **30**, 329 (1998).
 - [4] S. Succi, *The Lattice Boltzmann Equation: for Fluid Dynamics and Beyond* (Oxford University Press, Oxford, 2001).
 - [5] N. Sawant, B. Dorschner, and I. V. Karlin, *J. Fluid Mech.* **941**, A62 (2022).
 - [6] R. W. Nash, H. B. Carver, M. O. Bernabeu, J. Hetherington, D. Groen, T. Krüger, and P. V. Coveney, *Phys. Rev. E* **89**, 023303 (2014).
 - [7] E. Castro-Ávila, P. Margaretti, J. Harting, and J. Muñoz, *Phys. Rev. E* **110**, 025304 (2024).
 - [8] J. W. McCullough and P. V. Coveney, *Sci. Rep.* **14**, 11317 (2024).
 - [9] X. Shan, X.-F. Yuan, and H. Chen, *J. Fluid Mech.* **550**, 413 (2006).
 - [10] D. Wilde, A. Krämer, D. Reith, and H. Foysi, *Phys. Rev. E* **101**, 053306 (2020).
 - [11] M. Atif, M. Namburi, and S. Ansumali, *Phys. Rev. E* **98**, 053311 (2018).
 - [12] P. K. Kolluru, M. Atif, M. Namburi, and S. Ansumali, *Phys. Rev. E* **101**, 013309 (2020).
 - [13] C. Coreixas and J. Latt, *Phys. Fluids* **32** (2020).
 - [14] S. Zhao, G. Farag, P. Boivin, and P. Sagaut, *Phys. Fluids* **32** (2020).
 - [15] Y. Feng, P. Boivin, J. Jacob, and P. Sagaut, *J. Comput. Phys.* **394**, 82 (2019).
 - [16] M. H. Saadat, F. Bösch, and I. V. Karlin, *Phys. Rev. E* **99**, 013306 (2019).
 - [17] V. E. Ambrus and V. Sofonea, *Phys. Rev. E* **86**, 016708 (2012).
 - [18] N. Frapolli, S. S. Chikatamarla, and I. V. Karlin, *Phys. Rev. E* **90**, 043306 (2014).
 - [19] X. Shan and X. He, *Phys. Rev. Lett.* **80**, 65 (1998).
 - [20] U. Frisch, B. Hasslacher, and Y. Pomeau, *Phys. Rev. Lett.* **56**, 1505 (1986).

- [21] H. Chen, I. Goldhirsch, and S. A. Orszag, *J. Sci. Comput.* **34**, 87 (2008).
- [22] H. Chen and S. Orszag, *Philosophical Transactions of the Royal Society A: Mathematical, Physical and Engineering Sciences* **369**, 2176 (2011).
- [23] F. J. Alexander, S. Chen, and J. Sterling, *Phys. Rev. E* **47**, R2249 (1993).
- [24] X. Shan and X. He, *Phys. Rev. Lett.* **80**, 65 (1998).
- [25] S. S. Chikatamarla and I. V. Karlin, *Phys. Rev. E* **79**, 046701 (2009).
- [26] X. Shan, *Phys. Rev. E* **81**, 036702 (2010).
- [27] W. P. Yudistiawan, S. K. Kwak, D. V. Patil, and S. Ansumali, *Phys. Rev. E* **82**, 046701 (2010).
- [28] N. Frapolli, S. S. Chikatamarla, and I. V. Karlin, *Phys. Rev. Lett.* **117**, 010604 (2016).
- [29] G. Vahala, P. Pavlo, L. Vahala, and N. S. Martys, *Int. J. Mod. Phys. C* **9**, 1247 (1998).
- [30] M. Namburi, S. Krithivasan, and S. Ansumali, *Sci. Rep.* **6**, 27172 (2016).
- [31] N. Cao, S. Chen, S. Jin, and D. Martinez, *Phys. Rev. E* **55**, R21 (1997).
- [32] S. Ansumali and I. V. Karlin, *Phys. Rev. Lett.* **95**, 260605 (2005).
- [33] S. S. Chikatamarla and I. V. Karlin, *Phys. Rev. Lett.* **97**, 190601 (2006).
- [34] X. Li, Y. Shi, and X. Shan, *Phys. Rev. E* **100**, 013301 (2019).
- [35] X. He, S. Chen, and G. D. Doolen, *J. Comput. Phys.* **146**, 282 (1998).
- [36] M. Atif, P. K. Kolluru, C. Thantapanally, and S. Ansumali, *Phys. Rev. Lett.* **119**, 240602 (2017).
- [37] M. Atif, P. K. Kolluru, and S. Ansumali, *Phys. Rev. E* **106**, 055307 (2022).
- [38] S. A. Hosseini, M. Atif, S. Ansumali, and I. V. Karlin, *Comput. Fluids* **259**, 105884 (2023).
- [39] G. R. McNamara, A. L. Garcia, and B. J. Alder, *J. Stat. Phys.* **87**, 1111 (1997).
- [40] S. Ansumali and I. V. Karlin, *Phys. Rev. E* **62**, 7999 (2000).
- [41] B. M. Boghosian, J. Yepez, P. V. Coveney, and A. J. Wagner, *Proc. R. Soc. London, Ser. A* **457**, 717 (2001).
- [42] S. Ansumali and I. V. Karlin, *J. Stat. Phys.* **107**, 291 (2002).
- [43] F. Tosi, S. Ubertini, S. Succi, and I. V. Karlin, *J. Sci. Comput.* **30**, 369 (2006).
- [44] S. S. Chikatamarla, S. Ansumali, and I. V. Karlin, *Phys. Rev. Lett.* **97**, 010201 (2006).
- [45] S. Ansumali and I. V. Karlin, *Phys. Rev. E* **65**, 056312 (2002).
- [46] A. N. Gorban and D. Packwood, *Phys. Rev. E* **86**, 025701 (2012).
- [47] R. A. Brownlee, A. N. Gorban, and J. Levesley, *Phys. Rev. E* **75**, 036711 (2007).

- [48] C. B. Laney, *Computational Gasdynamics* (Cambridge University Press, 1998).
- [49] P. D. Lax and X.-D. Liu, SIAM J. Sci. Comput. **19**, 319 (1998).
- [50] P. D. Lax and X.-D. Liu, SIAM J. Sci. Comput. **19**, 319 (1998),
<https://doi.org/10.1137/S1064827595291819>.
- [51] C. W. Schulz-Rinne, J. P. Collins, and H. M. Glaz, SIAM J. Sci. Comput. **14**, 1394–1414 (1993).
- [52] A. Kurganov and E. Tadmor, J. Comput. Phys. **160**, 241 (2000).
- [53] D. Ghosh, <https://github.com/debog/hypar>.
- [54] N. Peng and Y. Yang, Phys. Rev. Fluids **3**, 013401 (2018).
- [55] S. Krithivasan, S. Wahal, and S. Ansumali, Phys. Rev. E **89**, 033313 (2014).
- [56] M. d. C. Henshaw, Verification and validation data for computational unsteady aerodynamics, 453 (2000).
- [57] J. Rossiter, (1964).
- [58] H. H. Heller, D. Holmes, and E. E. Covert, J. Sound Vib. **18**, 545 (1971).
- [59] P. K. Kolluru, M. Atif, and S. Ansumali, J. Comput. Sci. **45**, 101179 (2020).
- [60] P. K. Kolluru, M. Atif, and S. Ansumali, J. Fluid Mech. **963**, A7 (2023).